

# Warm gas in protostellar outflows

## I. Flows from the low-mass protostars in L1448 and HH211<sup>★,★★</sup>

A. I. Gomez-Ruiz<sup>1,2,\*\*\*</sup>, F. Wyrowski<sup>1</sup>, A. Gusdorf<sup>1,3</sup>, S. Leurini<sup>1</sup>, K. M. Menten<sup>1</sup>, and R. Güsten<sup>1</sup>

<sup>1</sup> Max-Planck-Institut für Radioastronomie (MPIfR), Auf dem Hügel 69, 53121 Bonn, Germany

<sup>2</sup> INAF, Osservatorio Astrofisico di Arcetri, Largo E. Fermi 5, 50125 Firenze, Italy  
e-mail: arturogr@arcetri.astro.it

<sup>3</sup> LERMA, UMR 8112 du CNRS, Observatoire de Paris, École Normale Supérieure, 24 rue Lhomond, 75231 Paris Cedex 5, France

Received 15 January 2012 / Accepted 3 April 2013

### ABSTRACT

**Context.** Observations of CO rotational transitions in the 0.3–0.4 millimeter range, now possible from exceptional sites on the ground, provide the opportunity of studying the warm component of molecular outflows in star-forming regions.

**Aims.** This study aims to characterize the role of the warm gas in high-velocity and collimated outflows from Class 0 low-mass protostars.

**Methods.** We used the CHAMP<sup>+</sup> heterodyne array on the APEX telescope to map the CO (6–5) and CO (7–6) emission in the well-known Class 0 outflows L1448-mm and HH211-mm. We complement these data with <sup>13</sup>CO (6–5) observations and also with previous low-*J* CO observations.

**Results.** The CO (6–5) and (7–6) emission was detected to be tracing the outflow lobes. In L1448, extremely high-velocity (EHV) emission was detected in both transitions. In HH211, high-velocity CO (6–5) emission was detected to be tracing the regions close to the central object, but it was also found close to the bow-shock regions seen in the mid-IR. A large velocity gradient code applied to these and the complementary low-*J* CO data revealed the high-velocity components to be dense ( $>10^5$  cm<sup>-3</sup>) and warm ( $T > 200$  K) gas, in agreement with previous observations of shock tracers such as SiO.

**Conclusions.** The high-velocity emission of these mid-*J* CO transitions are very good tracers of the inner highly excited part of outflows, which possibly is molecular material related to the underlying jet. In addition, these transitions are also strong at the bow-shock positions, which make them a good tool for probing these environments.

**Key words.** ISM: jets and outflows – stars: formation – ISM: individual objects: L1448 – ISM: individual objects: HH211 – shock waves

## 1. Introduction

Bipolar molecular outflows are a common phenomenon accompanying the formation of both low- and high-mass stars (Arce et al. 2007). The perturbation produced when outflow momentum and energy are injected into the material surrounding the protostar has an impact on the mass assembly process. Outflows are known to affect the material from the immediate vicinity of the protostar (core and envelope) up to cloud scales (tens of parsec), and therefore are most likely responsible for clearing surrounding material off the protostellar object, which induces the termination of the infall phase and affects the star formation efficiency (Arce et al. 2007). The high temperatures produced when the outflow impacts the interstellar medium give rise to chemical reactions that would not occur in the quiescent, dense interstellar medium (ISM), increasing the chemical complexity

in the affected gas. For all these reasons, molecular outflows are an important part of the star formation process.

Traditionally, molecular outflows have been studied through observations of low-*J* CO and low-*J* SiO rotational lines (low-*J* defined here as transitions up to  $J_u = 5$ ). The upper-state energies of these transitions imply that their excitation requires low gas temperatures. In the case of CO, transitions up to  $J_u = 4$ , with upper-state energies ( $E_u$ )  $< 50$  K, have been commonly used; for SiO transitions up to  $J_u = 5$ , with  $E_u \leq 40$  K, have been usually observed to trace the outflow gas. However, some studies exist of higher-*J* CO transitions (up to  $J_u = 38$ , from space facilities such as ISO and *Herschel*, e.g. Nisini et al. 2002; van Kempen et al. 2010a), as well as SiO transitions (up to  $J_u = 11$ , from ground-based facilities: Kawamura et al. 1999), probing temperatures  $\geq 100$  K. These observations have proven that these transitions are useful tools for tracing the warm and/or dense gas present within the shocked regions.

Recent studies by van Kempen et al. (2009b,a), using the CHAMP<sup>+</sup> array on the Atacama Pathfinder EXperiment (APEX) telescope, have shown the importance of mid-*J* CO transitions (throughout this paper referring to CO (6–5) and CO (7–6) transitions) in tracing the warm gas (50–200 K) in the envelope and outflow of low-mass protostars. These authors found a strong and narrow low-velocity CO (6–5) line around the central position and outflow regions of several low-mass objects, which they interpreted as emission originating from material heated by

\* Based on observations acquired with the Atacama Pathfinder Experiment (APEX). APEX is a collaboration between the Max-Planck-Institut für Radioastronomie, the European Southern Observatory, and the Onsala Space Observatory.

\*\* The high-velocity CO (6–5) maps of L1448 and HH211 are available at the CDS via anonymous ftp to [cdsarc.u-strasbg.fr](http://cdsarc.u-strasbg.fr) (130.79.128.5) or via <http://cdsarc.u-strasbg.fr/viz-bin/qcat?J/A+A/555/A8>

\*\*\* Member of the International Max-Planck Research School for Astronomy and Astrophysics at the Universities of Bonn and Cologne.

UV photons (which are most likely produced in the accretion shock) scattered in the outflow cavity, and not only by the passive heating taking place in the inner protostellar envelope. Since the low-velocity narrow component becomes stronger closer to the shocked region, it was suggested that this emission is enhanced by additional UV photons coming from the shocks. In addition, the emission from the broad wing component was consistent with temperatures  $\sim 100$  K. Although these observations provided information on the heating process close to the central object and a preliminary view of the role of shocks in the excitation of mid- $J$  CO transitions in outflows, they shed little light on the excitation of CO in the high-velocity material. In particular, these studies did not include outflows with extremely high-velocity (EHV) emission, since they were mainly focused on the quiescent emission from envelopes and low-velocity outflows. Recent CO (3–2) and SiO (8–7) observations of EHV outflows from class 0 protostars have suggested that these transitions may be tracing the material very close to the primary jet, probably the molecular counterpart of the atomic jet (Palau et al. 2006). Moreover, new submillimeter and far-IR observations of H<sub>2</sub>O and CO transitions in these kind of sources by Kristensen et al. (2011) have confirmed that these higher frequency lines trace outflow gas with high-excitation conditions ( $T_{\text{kin}} > 150$  K,  $n > 10^5$  cm<sup>-3</sup>). With all these informations it is clear that observations of mid- $J$  CO lines are important, because it is expected that their elevated excitation requirements would most directly make them probes of the primary jet. With the objective of studying the properties of the warm gas in EHV outflows, we have observed two well-known prototypes of such objects. In this paper we present CO (6–5) and (7–6) observations of two class 0 outflows with EHV emission and with a high collimation degree, L1448 and HH211.

## 2. The sources

### 2.1. The L1448-mm/IRS3 region

L1448 is a dense globule located in the nearby complex of dark clouds in Perseus (Bachiller & Cernicharo 1986), at a distance of 235 pc (Hirota et al. 2011). Associated with the globule are three IRAS sources, named IRS 1, 2, and 3; IRS3 being the most prominent source at infrared wavelengths (Bachiller & Cernicharo 1986). CO observations around IRS3 revealed high-velocity gas to the south of the infrared source (Bachiller et al. 1990). The high-velocity CO emission was found to be tracing a well-collimated and bipolar structure, with a terminal radial velocity of about  $\pm 70$  km s<sup>-1</sup> (with respect to the LSR velocity,  $V_{\text{LSR}}$ , of  $+4.5$  km s<sup>-1</sup>; Bachiller et al. 1990) and a size of  $\sim 4.5'$  (see Fig. 1). Along the main outflow axis, several well-defined CO clumps were found to be moving at high velocities, the so-called molecular “bullets”. These clumps appear at symmetrical positions with respect to a center ( $83''$  south of IRS3) that was later identified as a compact millimeter continuum source (Bachiller et al. 1991), with a bolometric luminosity  $L_{\text{bol}}$  of  $7.5 L_{\odot}$  (Tobin et al. 2007), named L1448-mm. In addition, the same CO observations also revealed a second (less energetic) outflow driven by IRS3 itself, orientated in a nearly east-west direction. To complicate matters, IRS3 turned out to be a binary system, that probably drives two bipolar outflows (e.g. Kwon et al. 2006). However, due to the overlap of IRS3 with the blueshifted lobe of L1448-mm outflow, a clear characterization of IRS3’s outflows has been difficult, even for interferometric observations (Kwon et al. 2006). Throughout the paper we refer to the region that includes the main outflow from L1448-mm and the outflow system around IRS3 as L1448-mm/IRS3.

The clump pairs in the L1448-mm main outflow, as traced by CO (2–1), were named B1-R1, B2-R2, B3-R3, and B4-R4, with “B” and “R” referring to blueshifted and redshifted clumps and with the numbering increasing going outward from L1448-mm (Bachiller et al. 1990, see Fig. 1a). At the highest velocities ( $V_{\text{LSR}} \sim -60$  and  $+70$  km s<sup>-1</sup>, for blue and redshifted emission) B1 and R1 appear in CO (2–1) as weak-intensity ( $T_{\text{MB}} \sim 0.1$  K) clumps within a region of  $\sim 10''$  in radius around L1448-mm, while farther away, B2-R2 show stronger CO (2–1) emission ( $T_{\text{MB}} \sim 1$  K). B3-R3 are similar to B2-R2 in intensity and size ( $\sim 20''$ ), although at slightly lower velocities than the later. B4-R4 are less well defined and appear at moderate radial velocities. At the lowest velocities the outflow lobes excited by IRS3 system can be seen. In this paper, we use the same terminology as based on the CO (2–1) observations by Bachiller et al. (1990) to name the clumps we found in CO (6–5).

### 2.2. HH211-mm

Located in the IC 348 complex in Perseus, at a distance of 250 pc (Enoch et al. 2006), the HH211 outflow was discovered from H<sub>2</sub> observations at  $2.12 \mu\text{m}$  (McCaughrean et al. 1994). The source driving this outflow was later identified with mm-wavelength continuum emission as a class 0 protostar with  $L_{\text{bol}} \sim 3.6 L_{\odot}$  (Froeblich 2005), known as HH211-mm. Follow-up CO observations showed that the low-velocity CO emission delineates a pair of cavities whose tips were associated with the  $2.12 \mu\text{m}$  H<sub>2</sub> emission. On the other hand, high-velocity CO traces a narrow jet-like structure along the axis of the cavities (Gueth & Guilloteau 1999, hereafter GG99). The high-velocity jet-like structure is also traced by SiO emission (e.g. Hirano et al. 2006). The total extent of the outflow is  $\sim 1.2'$ , with a terminal radial velocity of  $25$  km s<sup>-1</sup> on the blue lobe and  $35$  km s<sup>-1</sup> on the red lobe (with respect to the cloud  $V_{\text{LSR}}$  of  $+9.2$  km s<sup>-1</sup> Palau et al. 2006). The high-velocity emission consists of clump pairs (or “bullets”) that are symmetrically located at each side of the continuum source. These bullets pairs have been named in Hirano et al. (2006) as B1-R1, B2-R2, B3-R3, B4-R4, and B5-R5; with “B” and “R” referring to the blueshifted and redshifted clumps and the numbering increasing going outward from HH211-mm (see Fig. 1b). Additional clumps have been found in the CO emission close to the bow-shocks traced by H<sub>2</sub> (Palau et al. 2006; Lee et al. 2007). In this paper we use the same terminology as defined for the low- $J$  CO and SiO observations by Hirano et al. (2006) and Palau et al. (2006) to name the clumps found in CO (6–5).

Recently, interferometric CO (3–2) and SiO (8–7) submillimeter observations have been performed in HH211-mm (Hirano et al. 2006; Palau et al. 2006). A comparison between the CO (3–2) and SiO (8–7) high-velocity emission with lower- $J$  CO (2–1) and SiO (1–0) has shown that submillimeter transitions trace the knots of gas very close to the exciting source better than the low- $J$  millimeter transitions. In particular, the B1-R1 clump pairs revealed in CO (3–2) and SiO (8–7) have no counterparts in CO (2–1) and SiO (1–0). Given the high densities and temperatures inferred for these high-velocity clumps close to the central position, it has been suggested that submillimeter CO and SiO transitions may be tracing the gas closely related with the primary jet (Hirano et al. 2006).

## 3. CHAMP+ observations at APEX

Mid- $J$  CO observations were performed with the MPIfR Principal Investigator (PI) instrument CHAMP+ (Kasemann et al. 2006) on the APEX telescope (Güsten et al. 2006).

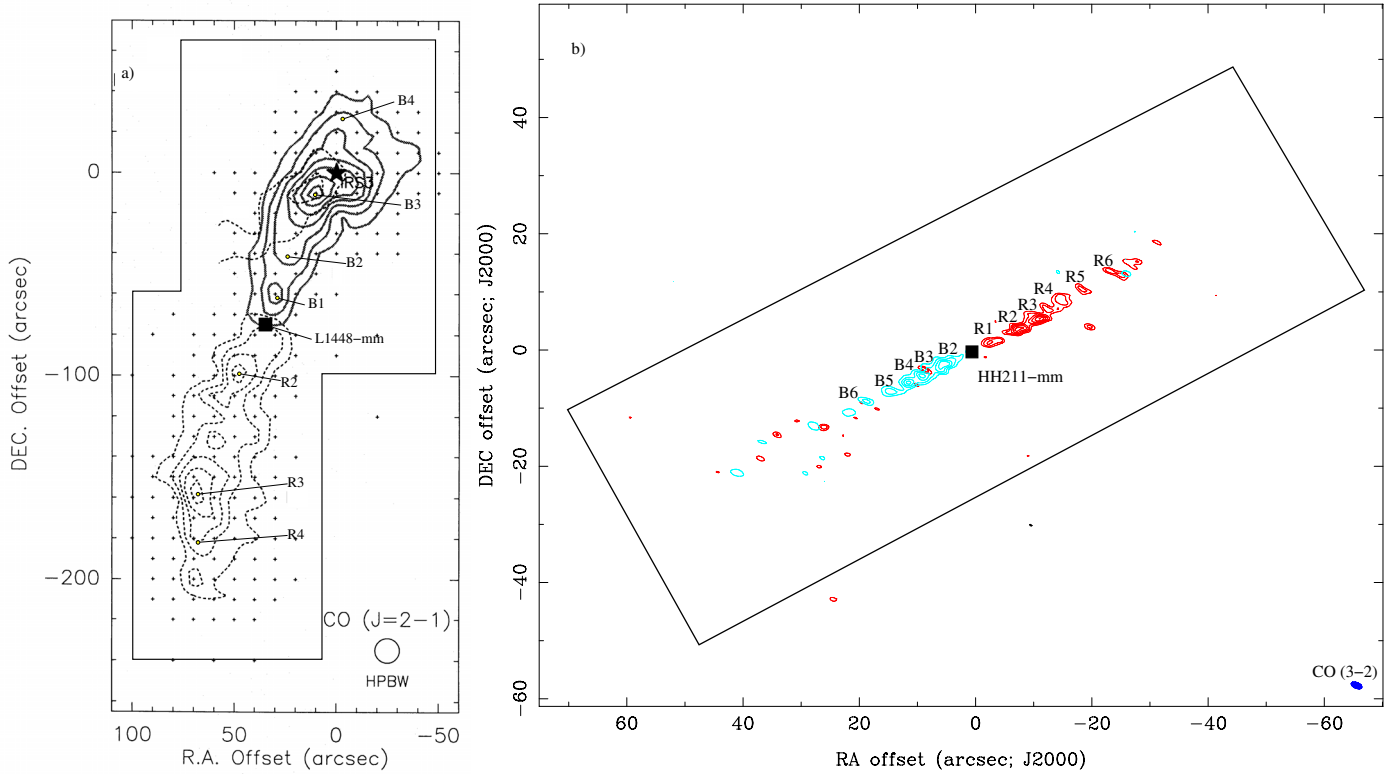


**Fig. 1.** **a)** CO (2–1) high-velocity emission in the L1448/IRS3 system, taken from [Bachiller et al. \(1990\)](#). The contours show the integrated emission in the ranges from  $-55 \text{ km s}^{-1}$  to  $0 \text{ km s}^{-1}$  (solid) and from  $+10 \text{ km s}^{-1}$  to  $+65 \text{ km s}^{-1}$  (dashed). First contour and contour interval are  $10 \text{ K km s}^{-1}$ . The central (0, 0) offset position is located at the position of IRS3 (black star), while the position of L1448-mm source is shown by the black square. The labels indicate the position of all clumps reported by [Bachiller et al. \(1990\)](#). **b)** The CO (3–2) high-velocity emission in HH211 taken from [Palau et al. \(2006\)](#). The contours show the integrated emission in the ranges from  $-14 \text{ km s}^{-1}$  to  $0 \text{ km s}^{-1}$  (blue) and from  $+20 \text{ km s}^{-1}$  to  $+40 \text{ km s}^{-1}$  (red). The contour interval is  $2\sigma$ , while first contour is  $4\sigma$  ( $\sigma = 2.21$  and  $2.38 \text{ Jy beam}^{-1} \text{ km s}^{-1}$ , for blue- and redshifted, respectively). The central (0, 0) offset position is located at the position of H211-mm (black square). The labels indicate the position of all clumps reported by [Palau et al. \(2006\)](#) and [Hirano et al. \(2006\)](#). In **a)** and **b)**, the beam of each observation is shown at the bottom-right, while the black polygons delineate approximately the area covered by the CO (6–5) and (7–6) observations.

CHAMP<sup>+</sup> is a dual-color  $2 \times 7$  pixel heterodyne array for operation in the  $450 \mu\text{m}$  (low-frequency array, LFA) and  $350 \mu\text{m}$  (high-frequency array, HFA) atmospheric windows. The optics allow simultaneous observations in both colors. Both subarrays present an hexagonal arrangement. The frontend is connected to a suit of fast Fourier-transform spectrometer (FFTS: [Klein et al. 2006](#)).

L1448-mm/IRS3 was observed in CO (6–5), (7–6) and  $^{13}\text{CO}$  (6–5) during 2009 June and August. HH211-mm was observed in the same transitions during 2010 July and September. The whole extent of the outflow of the two sources was mapped (blue and red lobes) simultaneously in CO (6–5) and (7–6). For L1448-mm/IRS3 a second setup was used to map only the central and northern part of the region, simultaneously in  $^{13}\text{CO}$  (6–5) and CO (7–6); while toward HH211-mm outflow single-pointing observations were performed on selected positions in a third setup consisting of  $^{13}\text{CO}$  (6–5) and  $\text{HCO}^+$  (9–8). For the purpose of this paper, the  $\text{HCO}^+$  (9–8) observations were not considered because of their low signal-to-noise ratio. For all observations, the backend was set with two overlapping units, of  $1.5 \text{ GHz}$  and  $8192$  channels each, that in the end provided a total bandwidth of  $2.8 \text{ GHz}$ . The final spectra were resampled to  $1 \text{ km s}^{-1}$  spectral resolution for all transitions in the sources.

During the observations, the precipitable water vapor (PWV) was in the range of  $0.3$  to  $0.7 \text{ mm}$ . The pointing was determined by CO (6–5) cross-scan observations on IK Tau

(L1448-mm/IRS3) and CRL618 (HH211-mm). Pointing corrections were always within  $3''$ . Focus was checked on Mars. Mapping observations were made in the on-the-fly mode, with an ON time of  $0.5 \text{ s}$  per position, and steps of  $3''$ . In the case of L1448-mm/IRS3, the reference position was observed without showing emission of the CO (6–5) line. On the other hand, for HH211-mm we did not observe the reference position, and because at emission-free positions in our map we could see absorption features at the cloud velocity, our spectra are contaminated at least at cloud velocities. Spectra were reduced with CLASS and images were produced with GREG; these softwares are part of the GILDAS package<sup>1</sup>. During the June 2009 observations an anomaly in the warm optics affected the coupling efficiency of the LFA, requiring the application of a correction factor depending on the dewar angle of the array during the observations. In addition, due to weather instabilities that affected the baseline stability of the high-frequency observations, a quarter of the CO (7–6) spectra in L1448 were unusable, affecting uniformly each point of the map. Tables 1 and 2 show a summary of the observations, including the transitions observed and the coordinates ( $\alpha/\delta$ ) of the central positions of the maps presented in this paper.

Intensities in this paper are presented in  $T_{\text{MB}}$  scale for which we have used a forward efficiency of  $0.95$  and beam efficiencies ( $\eta_s$ ) measured on Jupiter. We consider the later appropriate based

<sup>1</sup> <http://iram.fr/IRAMFR/PDB/gildas/gildas.html>

**Table 1.** Transitions observed.

Line	$\nu_0$ GHz	$A$ $10^{-5} \text{ s}^{-1}$	$E_u/k$ K	HPBW ''	$\eta_s$ a
CO (6–5)	691.473	2.137	116.16	9.0	0.46
CO (7–6)	806.651	3.422	154.87	7.7	0.40
$^{13}\text{CO}$ (6–5)	661.067	1.868	111.05	9.4	0.46

**Notes.** (a) Values measured during L1448/IRS3 observations. See text for details and for the values during HH211 observations.

**Table 2.** Source information and map rms.

Source	$\alpha$ (J2000) (h m s)	$\delta$ (J2000) ( $^{\circ}$ ' '')	$V_{\text{LSR}}$ ( $\text{km s}^{-1}$ ) <sup>a</sup>	$^{12}\text{CO}$ rms (K) <sup>b</sup> (6–5)	(7–6)
L1448-mm	03:25:38.9	30:44:05.0	+4.5 <sup>c</sup>	0.31	0.88
HH211-mm	03:43:56.8	32:00:50.0	+9.2 <sup>d</sup>	0.66	0.21

**Notes.** (a) Bandpass center. (b) Average rms, in  $T_{\text{MB}}^*$ , at  $1 \text{ km s}^{-1}$  spectral resolution. (c) [Bachiller et al. \(1990\)](#). (d) [Palau et al. \(2006\)](#).

on the average size of the structures we have mapped in both outflows. During the L1448-mm observations,  $\eta_s$  values measured on Jupiter were 0.46 and 0.40, for LFA and HFA, respectively. During the HH211-mm observations,  $\eta_s$  of 0.48 was measured for both LFA and HFA. Unless otherwise stated, throughout the paper an LSR velocity is used to present and describe the data.

## 4. Molecular outflows in L1448-mm/IRS3

### 4.1. High-velocity CO (6–5) emission

The CO (6–5) emission was detected in a velocity range from  $-60$  to  $+70 \text{ km s}^{-1}$ . Figure 2 shows the CO (6–5) emission in L1448-mm/IRS3, integrated over the red- and blueshifted wings. The overall morphology is similar to the structures traced by previous low- $J$  CO observations. Redshifted emission mainly traces a curved-like structure that forms the red lobe located to the southeast of L1448-mm. To the northwest of the central position a blueshifted lobe terminates around the position of IRS3. Close to the position of IRS3 one also notes a redshifted clump that, together with a blueshifted elongated feature to the west, delineates the outflow system from IRS3. The integrated intensity map shows that the CO (6–5) brightness distribution is more prominent within the inner  $20''$  around L1448-mm and around IRS3. Moreover, the redshifted lobe from L1448-mm shows weaker emission than the blueshifted lobe.

Figure 3 presents the CO (6–5) emission integrated in intervals of  $10 \text{ km s}^{-1}$ , from high to low velocities, overlaid on the  $4.5 \mu\text{m}$  mid-IR emission from *Spitzer*/IRAC, which is thought to trace shocked regions ([Smith et al. 2006](#); [Tobin et al. 2007](#); [Neufeld et al. 2009](#)). Most of the clumps previously found in low- $J$  CO are present at the velocity intervals of the CO (6–5) emission, showing the characteristic blue-red correspondence. At high velocities, the clumps with the strongest emission are B1-R1 ( $T_{\text{MB}} \sim 1 \text{ K}$ ). The B2-R2 clumps are weakly detected at their nominal velocities; indeed R2 is barely detected in the interval between  $+60 \text{ km s}^{-1}$  to  $+50 \text{ km s}^{-1}$ . This behavior is the opposite to low- $J$  CO (2–1) emission, in which B2-R2 are stronger than B1-R1 at such high velocities. In addition, B4, a clump detected in CO (2–1) around  $-40 \text{ km s}^{-1}$  to  $-20 \text{ km s}^{-1}$  (see [Bachiller et al. 1990](#)), is not detected in our CO (6–5) observations in that velocity range. The remaining clumps (B3-R3 and R4) present a similar behavior in the CO (6–5) as in the

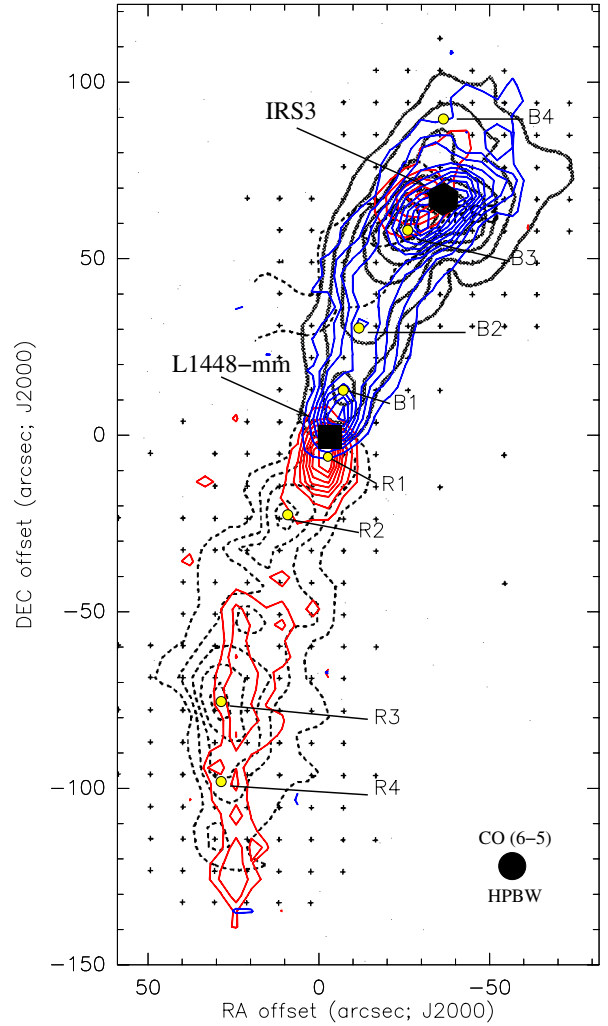


**Fig. 2.** CO (6–5) high-velocity emission in the L1448-mm/IRS3 system. Blue contours show the blueshifted wing (from  $-55 \text{ km s}^{-1}$  to  $0 \text{ km s}^{-1}$ ) and red contours the redshifted wing (from  $+10 \text{ km s}^{-1}$  to  $+65 \text{ km s}^{-1}$ ). The contour spacing is  $2\sigma$ , with the first contour at  $3\sigma$  ( $\sigma = 3.95 \text{ K km s}^{-1}$  for blue and  $\sigma = 5.65 \text{ K km s}^{-1}$  for red). The central (0,0) position is located at the coordinates of L1448-mm source (see Table 2) and indicated by the black square. The black hexagon represents the position of IRS3 (offset  $-38, +70$ ). Black contours (solid and dashed) show the CO (2–1) emission from [Bachiller et al. \(1990\)](#), integrated in the same velocity ranges. The black crosses indicate the coverage of the CO (2–1) map, which is roughly identical in CO (6–5). Yellow circles indicate the positions of all clumps reported by [Bachiller et al. \(1990\)](#). Also shown with a black filled circle is the HPBW at the frequency of the CO (6–5) transition.

(2–1) line. In Table 3 we report the position of the clumps obtained by a two-dimensional Gaussian fit to the CO (6–5) maps. For the Gaussian fits we used the velocity interval from Fig. 3, in which the clumps are strongest. Table 3 also shows the deconvolved minor and major axis of the Gaussian fits and their position angle (PA). As revealed by the deconvolved sizes, the high-velocity emission from B1/R1 is not resolved in the direction perpendicular to the jet axis. The clumps farther away from the central position (e.g. R3, R4) are partially or fully resolved in the  $9.0''$  FWHM beam.

The last two lower velocity panels in Fig. 3 show the low-velocity CO (6–5) emission. At these velocities, outflow from IRS3 is seen mixed with emission from the B3 clump of the L1448-mm outflow. At the velocity intervals centered at  $-15$  and  $+25 \text{ km s}^{-1}$ , two compact clumps (blue- and redshifted

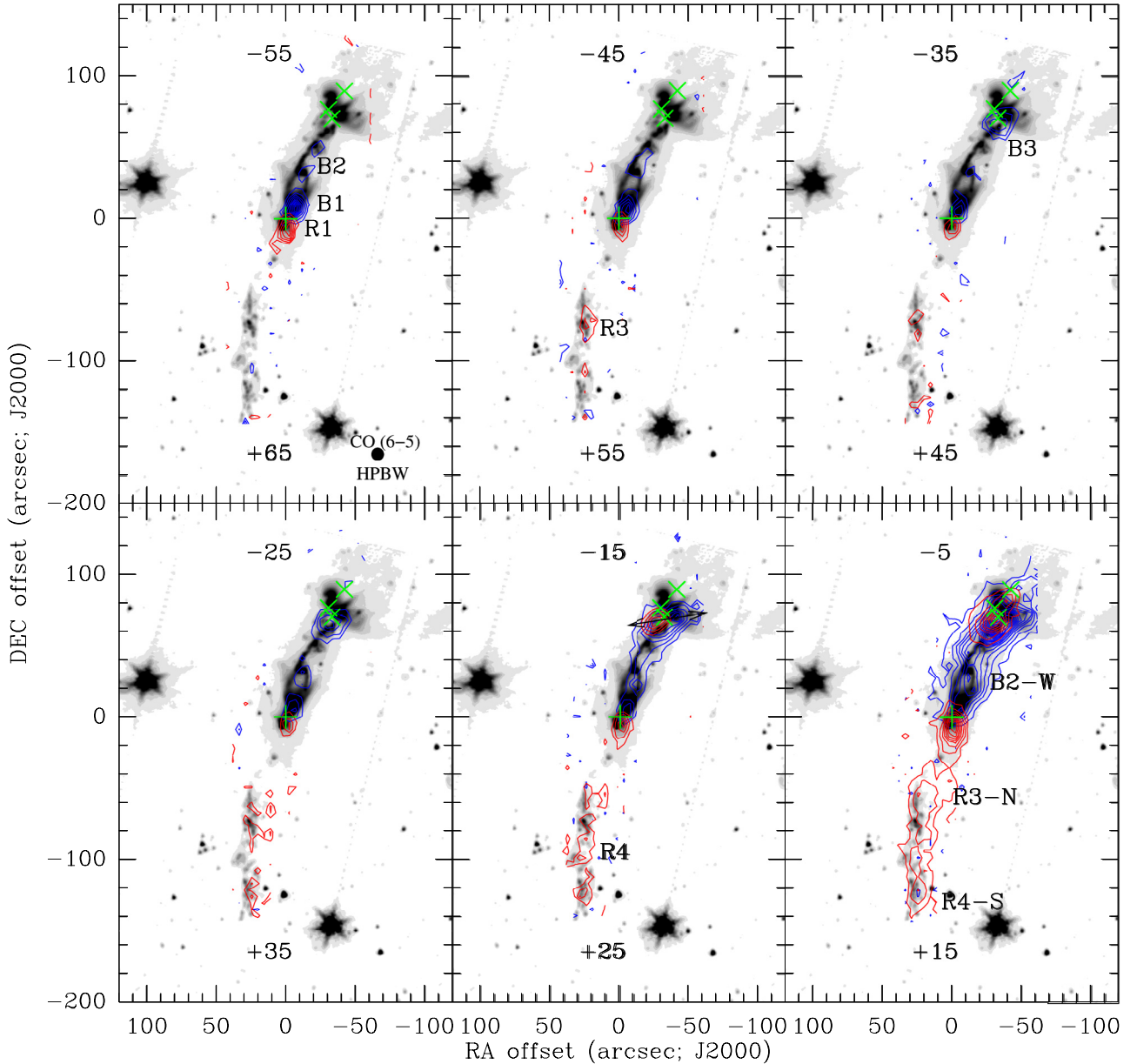


**Fig. 3.** CO (6–5) maps of the L1448-mm/IRS3 region in different velocity ranges, overlaid on the *Spitzer*/IRAC 4.5  $\mu\text{m}$  image. Each panel shows the integrated red- and blueshifted emission in a  $10 \text{ km s}^{-1}$  wide velocity interval, centered on the velocity shown in the bottom (redshifted) and top (blueshifted) part of each panel. The contour spacing is  $2\sigma$ , with the first contour at  $3\sigma$  ( $\sigma = 1.20 \text{ K km s}^{-1}$  for blue contours and  $\sigma = 1.61 \text{ K km s}^{-1}$  for red contours). The (0, 0) offset refers to the position of L1448-mm central source (see Table 1), also indicated by a green plus symbol. The green crosses represent the position of the members of the IRS3 system (3A, 3B, and 3C; Kwon et al. 2006) The arrow in the *bottom-middle panel* indicates the direction of the outflow system from IRS3. The peak values for the highest velocity range are  $11.3 \text{ K km s}^{-1}$  for B1 and  $10.3 \text{ K km s}^{-1}$  for R1.

clumps) are oriented in an almost east-west direction, probably tracing the high-velocity part of IRS3 outflow (marked by an arrow in Fig. 3).

#### 4.2. Low-velocity CO (6–5) emission

In Fig. 4 we show the low-velocity channels in bins of  $1 \text{ km s}^{-1}$  of the CO (6–5) emission in L1448-mm/IRS3. The outflow structures are clearly recognized in all low-velocity channels. A rich clumpy structure is visible around the blue lobe of L1448-mm and IRS3 system (see, e.g., 2 and  $3 \text{ km s}^{-1}$  channels). A more diffuse and extended emission is also noted especially in the couple of channels around the cloud velocity (4 and  $5 \text{ km s}^{-1}$  channels). Several of the clumps observed in these low-velocity channels did not have counterparts at high velocities. These

clumps are named B2-W and B3-S for the L1448 outflow, and IRS3-B1, IRS3-B2, IRS3-R1, and IRS3-R2 for the clumps related to the outflows excited by IRS3. The positions of these low-velocity clumps are also shown in Table 3.

#### 4.3. CO (6–5) line profiles

Figure 5 shows a sample of spectra at different positions in L1448-mm/IRS3. Similar to previous low- $J$  CO observations, several spectral features are present. First, the peak of the CO emission at the cloud velocity ( $V_{\text{LSR}} = 4.5 \text{ km s}^{-1}$ ), which is present in all positions shown in Fig. 5. Second, the high-velocity broad wing, extending from  $-65 \text{ km s}^{-1}$  to  $\sim +75 \text{ km s}^{-1}$ . The third component is represented by the

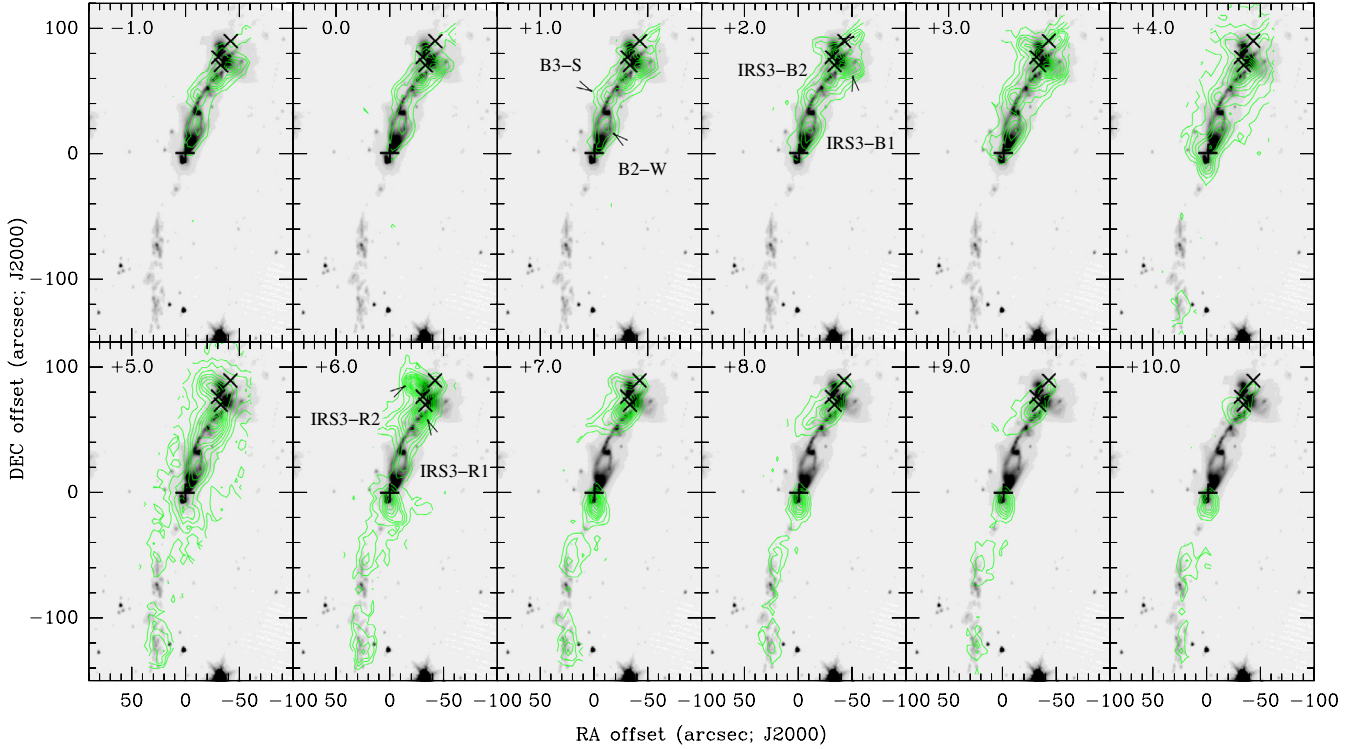


**Fig. 4.** CO (6–5) low-velocity channel maps in L1448-mm/IRS3 region. Contours spacing is  $2\sigma$ , with the first contour at  $3\sigma$  ( $\sigma = 0.62 \text{ K km s}^{-1}$ ). The plus symbol and crosses represent the continuum sources as in Fig. 3. The arrows indicate the clumps that are traced only at low velocities (positions reported in Table 3).

**Table 3.** Clump characteristics derived from the CO (6–5) emission.

Clump	Velocity <sup>+</sup> range (km s <sup>-1</sup> )	Offset (" , ")	$\alpha$ (J2000) h m s	$\delta$ (J2000) ° ' "	Deconvolved		PA (°)	$\int T_{\text{MB}} d\theta^*$ K km s <sup>-1</sup>
					Major axis (")	Minor axis (")		
L1448-mm								
B1	-75, 26	-6.9, 7.6	03:25:38.3	30:44:12.68	11.6	4.2	-17.5	103.7(1.4)
R1	-19, 85	-1.0, -7.6	03:25:38.8	30:43:57.30	11.7	2.5	-15.3	146.1(1.7)
B2	-75, 12	-13.4, 34.1	03:25:37.8	30:44:39.10	16.7	12.2	-9.8	70.2(1.1)
B2-N	-73, 40	-21.6, 46.4	03:25:37.2	30:44:51.43	18.2	8.7	-33.6	81.6(1.1)
B2-W	-78, 10	-8.8, 16.2	03:25:38.2	30:44:21.23	46.5	15.6	-30.4	77.2(1.2)
R2	-1, 80	7.3, -21.1	03:25:39.4	30:43:43.82	<i>a</i>	<i>a</i>	<i>a</i>	38.4(2.2)
B3	-52, 52	-34.6, 66.5	03:25:36.2	30:45:11.56	18.5	13.3	-69.4	185.8(1.1)
B3-S	-33, 17	-12.7, 46.1	03:25:37.9	30:44:51.13	28.5	17.5	-36.8	72.6(1.0)
R3	-1, 66	22.9, -73.6	03:25:40.6	30:42:51.31	24.7	9.7	4.3	40.1(1.9)
R3-N	0, 68	18.9, -50.3	03:25:40.3	30:43:14.63	36.0	20.2	-17.1	49.7(1.9)
R4	0, 66	27.1, -93.8	03:25:41.0	30:42:31.20	35.9	16.7	-23.9	33.1(2.3)
R4-S	-1, 60	25.1, -117.4	03:25:40.8	30:42:07.50	42.5	16.8	6.7	54.8(3.0)
IRS3								
IRS3-B1	-40, 20	-41.6, 68.5	03:25:35.6	30:45:13.58	19.3	12.4	86.0	158.1(2.5)
IRS3-R1	-47, 35	-28.4, 62.6	03:25:36.6	30:45:07.64	30.2	13.6	-39.4	209.8(2.3)
IRS3-B2	-5, 8	-52.0, 89.6	03:25:34.8	30:45:34.66	26.4	11.5	-38.3	36.7(1.8)
IRS3-R2	-8, 15	-28.6, 82.7	03:25:36.6	30:45:27.74	26.7	11.3	59.2	60.7(1.4)
IRS3-B3	-33, 26	-29.9, 58.8	03:25:36.5	30:45:03.89	16.0	13.9	-46.2	180.5(2.0)
HH211-mm								
B1-B2-B3	-10, 15	11.6, -3.7	03:43:57.6	32:00:46.23	19.8	4.3	-66.7	75.6(0.6)
R1-R2-R3	3, 45	-7.2, 6.3	03:43:56.2	32:00:56.38	21.0	1.4	-58.2	72.9(1.6)
B7	-3, 16	29.0, -10.1	03:43:59.0	32:00:39.82	22.0	3.1	-78.6	70.0(1.3)
R6	4, 17	-22.0, 14.1	03:43:55.0	32:01:04.10	20.1	3.5	-73.1	45.3(1.0)

**Notes.** <sup>(a)</sup> convolution seems to produce a point source. <sup>+</sup> Total velocity range of the emission at  $3\sigma$  level. <sup>(\*)</sup> Total integrated emission within the specified velocity range.

so-called EHV bullets, which are shown in the spectrum around the L1448-mm, B1, and R1 positions as secondary peaks at  $\sim -60 \text{ km s}^{-1}$  in the blue lobe and  $\sim +70 \text{ km s}^{-1}$  in the red lobe.

The characteristic shock profile at the positions R2, B2, and R3 is also remarkable. This profile is represented by a peak at low velocities, with a gradual decrease of the intensity toward high

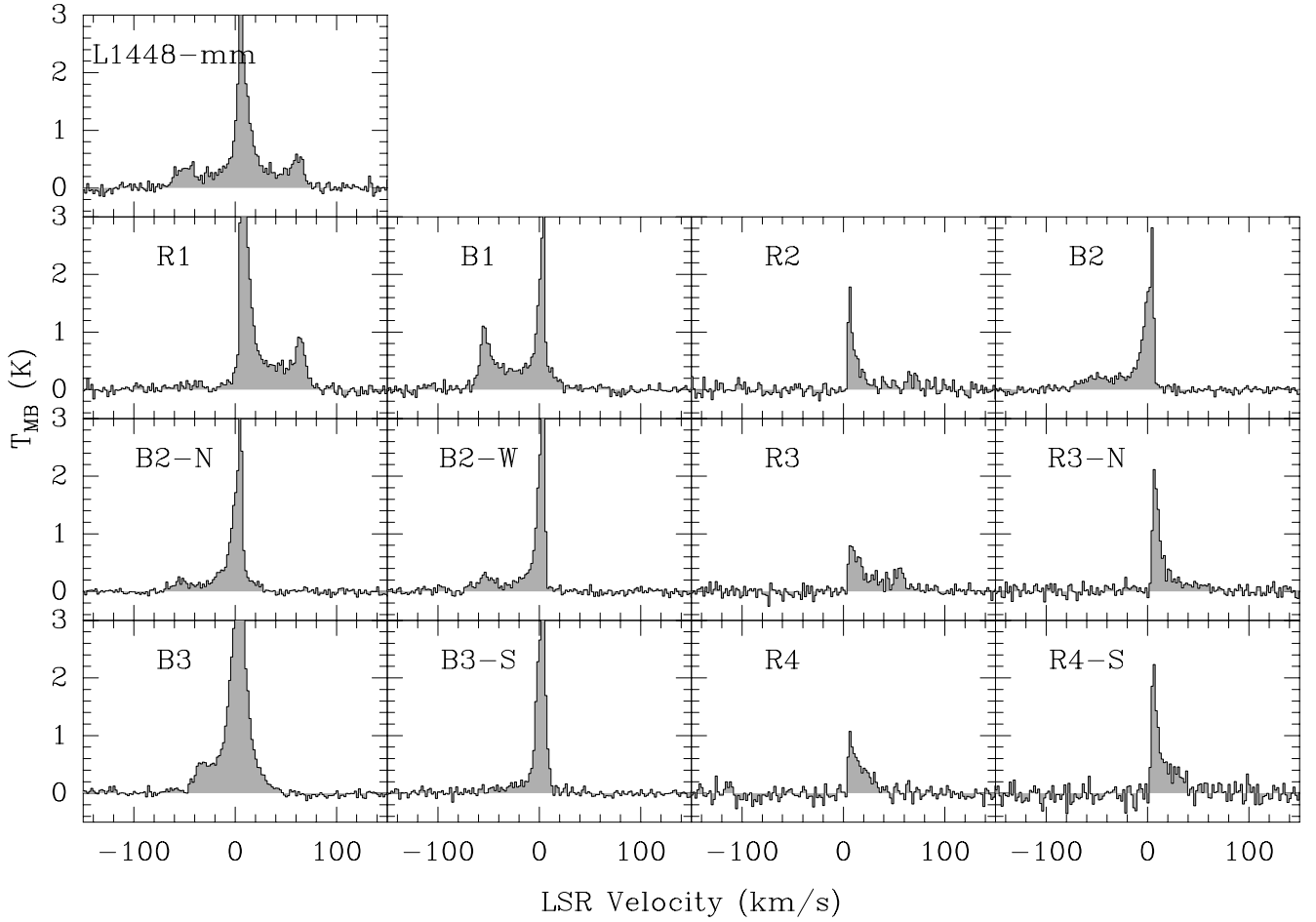


**Fig. 5.** CO (6–5) spectra at the positions indicated in Fig. 3. The spectral resolution is  $1 \text{ km s}^{-1}$ . Upper left corner of each panel indicates the position at which the spectrum was taken.

velocities, while a sharp decrease in intensity is seen toward low velocities (Schilke et al. 1997).

#### 4.4. $^{13}\text{CO}$ (6–5) and CO (7–6)

The  $^{13}\text{CO}$  (6–5) map of L1448-mm/IRS3 includes the positions L1448-mm, R1, B1, R2, B2, B2-W, B2-N, B3, B3-S, and IRS3. Due to time constraints and because the  $^{12}\text{CO}$  (6–5) emission was found to be weaker toward the red lobe, the remainder of this lobe was not covered by the  $^{13}\text{CO}$  (6–5) map. The integrated intensity  $^{13}\text{CO}$  (6–5) map is presented in Fig. 6 while the spectra at selected positions are shown in Fig. 7. The  $^{13}\text{CO}$  (6–5) emission was clearly detected only toward L1448-mm, R1, R2, B3, and IRS3. Marginal detections ( $\sim 2\sigma$ ) are reported in B1, B2-N, B2-W, and B3-S. No detection was made in B2. Throughout, the  $^{13}\text{CO}$  (6–5) emission is only detected in one to three channels around the systemic velocity.

On the other hand, owing to the simultaneous observations with the CO (6–5) line, the CO (7–6) map covered the entire L1448/IRS3 system. The integrated intensity CO (7–6) map is shown in Fig. 6 and the CO (7–6) spectra at selected positions are shown in Fig. 8. The CO (7–6) emission was found mostly at low velocities. However, at the L1448-mm, B1, and R1 positions, the CO (7–6) emission is detected at extremely high velocities (at a  $6\sigma$  level). The total integrated emission is dominated by the low-velocity gas. The low velocity-emission is stronger around L1448-mm (including R1, B1, and B2 clumps) and around IRS3 (see Fig. 6).

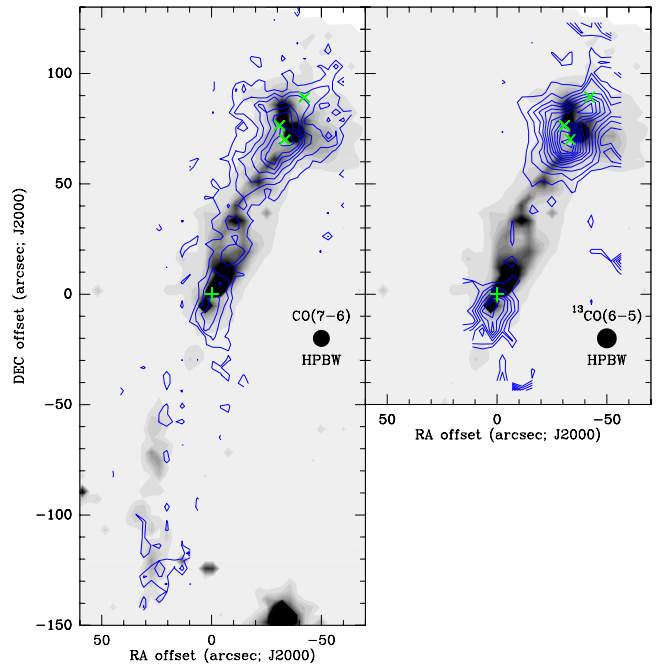


**Fig. 6.** Integrated CO (7–6) (left panel) and  $^{13}\text{CO}$  (6–5) (right panel) emission in L1448-mm/IRS3. Contours start at  $3\sigma$  and then are spaced in steps of  $2\sigma$  for both CO (7–6) and  $^{13}\text{CO}$  (6–5).  $\sigma = 8.55 \text{ K km s}^{-1}$  for CO (7–6) and  $\sigma = 0.62 \text{ K km s}^{-1}$  for  $^{13}\text{CO}$  (6–5). The green plus symbol and crosses are the same as in Fig. 3.

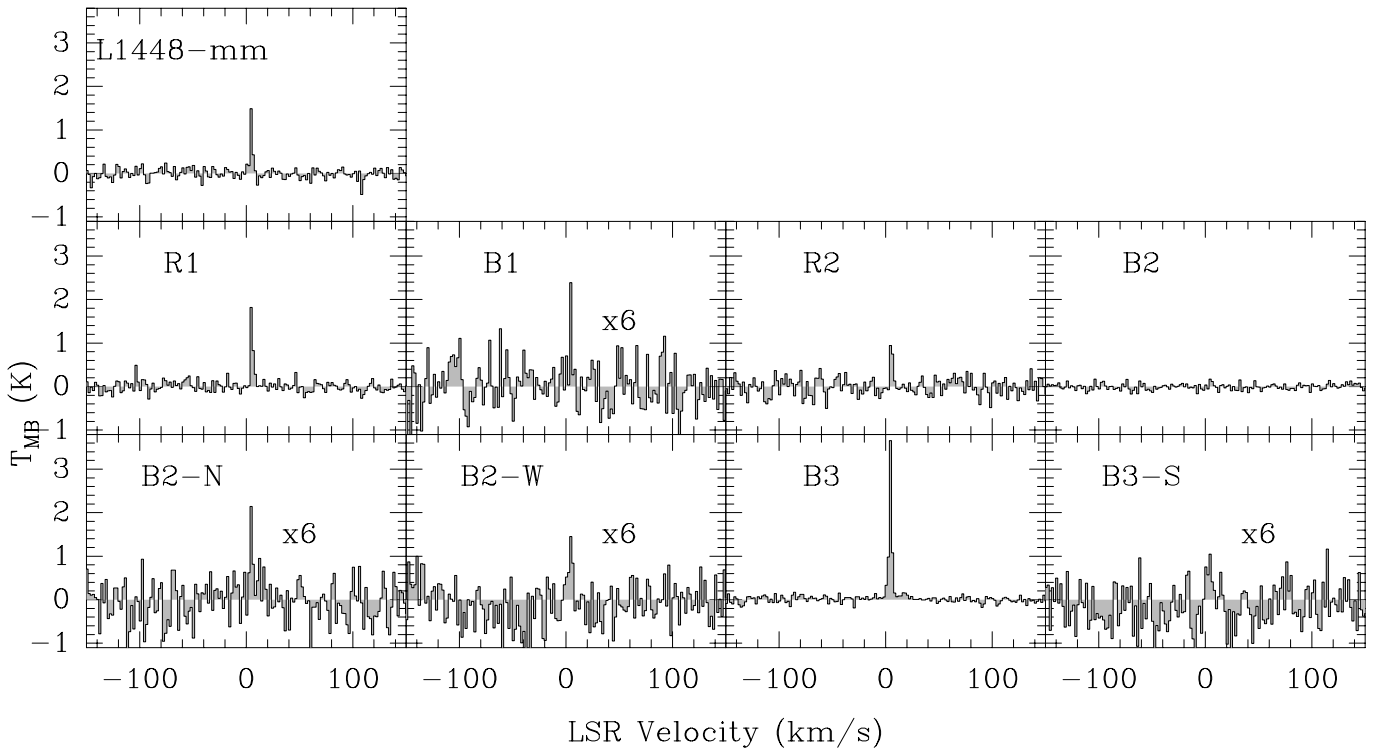


**Fig. 7.**  $^{13}\text{CO}$  (6–5) spectra at the observed positions in L1448/IRS3. The positions are indicated in each panel. The spectral resolution is  $1 \text{ km s}^{-1}$ .

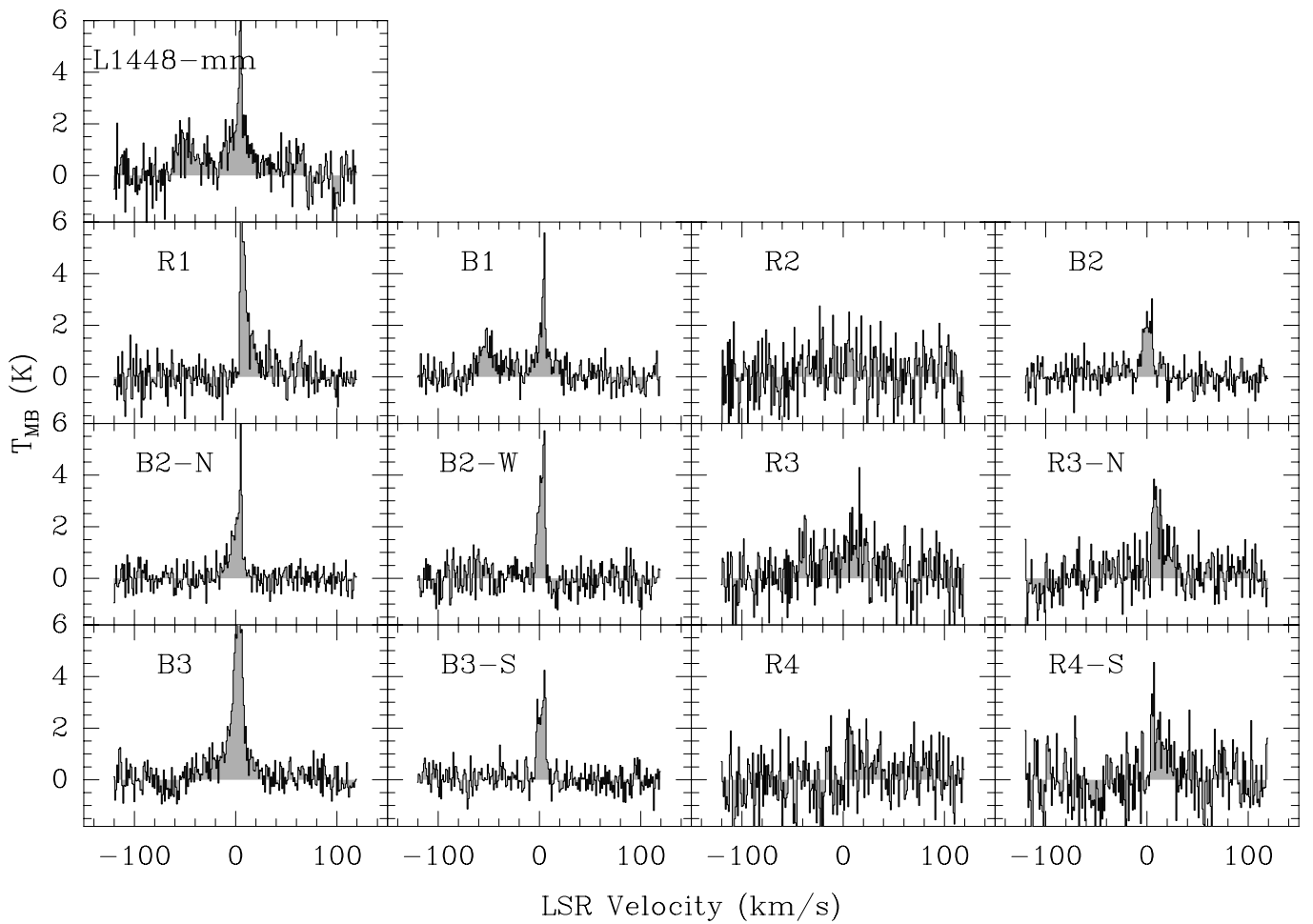


**Fig. 8.** CO (7–6) spectra at the observed positions in L1448/IRS3. The positions are indicated with labels in each panel. The spectral resolution is  $1 \text{ km s}^{-1}$ .

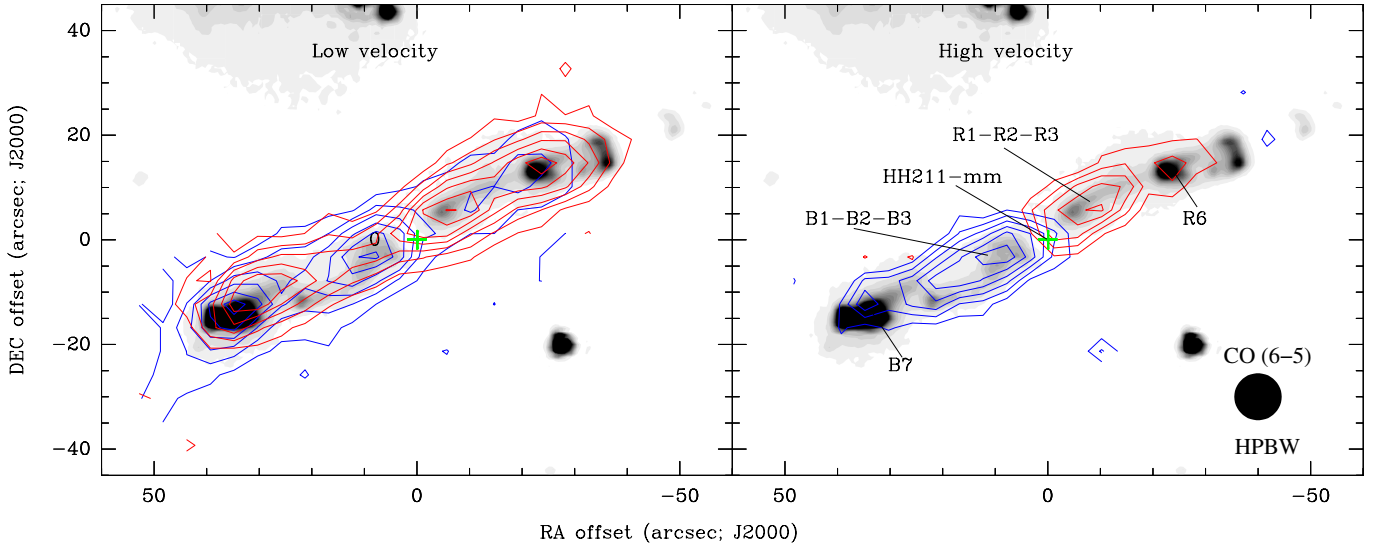


**Fig. 9.** CO (6–5) emission in HH211 overlaid on the *Spitzer*/IRAC 4.5  $\mu\text{m}$  emission. *Left*: integrated low-velocity emission (2 to 8  $\text{km s}^{-1}$  [blue] and 10 to 18  $\text{km s}^{-1}$  [red]). *Right*: integrated high-velocity emission (–15 to 1  $\text{km s}^{-1}$  [blue] and 19 to 41  $\text{km s}^{-1}$  [red]). For low-velocity emission the contour spacing is  $3\sigma$ , with the first contour at  $3\sigma$  ( $\sigma = 1.74 \text{ K km s}^{-1}$ ). For the high-velocity emission the contour spacing is  $2\sigma$ , with the first contour at  $3\sigma$  ( $\sigma = 1.98 \text{ K km s}^{-1}$  for blue and  $\sigma = 2.37 \text{ K km s}^{-1}$  for red). The green plus symbol indicates the position of HH211-mm source, located at offset (0, 0) (see Table 1). Also shown by a black circle is the HPBW at the frequency of the CO (6–5) transition.

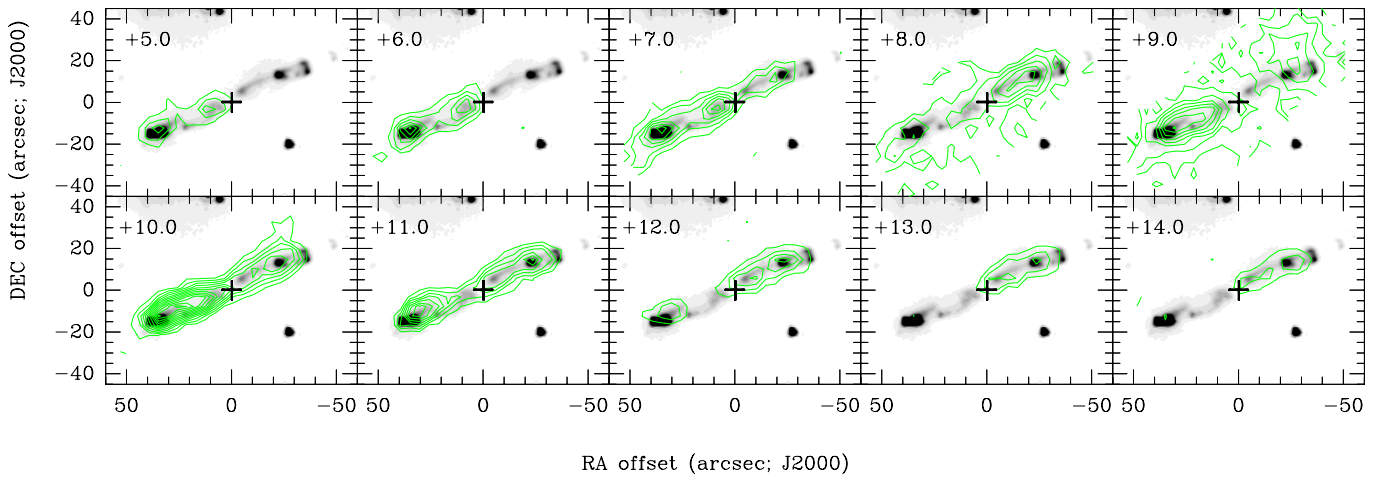


**Fig. 10.** CO (6–5) low-velocity channel maps in HH211-mm. The contours spacing is  $2\sigma$ , with the first contour starting at  $3\sigma$  ( $\sigma = 0.79 \text{ K km s}^{-1}$ ). The plus symbol indicates the position of the central source as in Fig. 9.

## 5. The HH211 molecular outflow

### 5.1. High-velocity CO (6–5) emission

The CO (6–5) emission in HH211 was detected from –14 to +42  $\text{km s}^{-1}$ . Figure 9 shows the CO (6–5) integrated intensity maps at low- and high velocities overlaid on the 4.5  $\mu\text{m}$  IRAC/Spitzer emission as a reference for shocked gas (Smith et al. 2006; Neufeld et al. 2009). The low-velocity emission (from 2 to 18  $\text{km s}^{-1}$ ) shows a shell-like structure surrounding the mid-IR features, but also noted are well-defined peaks coincident with the mid-IR knots around the bow-shocks. On the other hand, at high velocities the CO (6–5) emission peaks close to the central source, but also near the bow-shocks traced by the mid-IR emission. We note that our CO (6–5) observations cannot spatially resolve the individual clumps close to the central source. In particular, the inner bullets, B1, B2, B3 and R1, R2, and R3, are shown as a single pair of knots in our CO (6–5) map. We refer to these knots as B1-B2-B3 and R1-R2-R3 in

Fig. 9. Since in previous low- $J$  CO observations the clumps at the mid-IR bow-shock positions were not named, we call them B7 and R6, following the notation from previous works. Interestingly, these clumps at the mid-IR bow-shocks showed weaker emission in CO (3–2) than in our CO (6–5) observations (e.g. Palau et al. 2006; Lee et al. 2007). All clump positions are reported in Table 3. In general, the morphology of the CO (6–5) emission is similar to that seen in low- $J$  CO observations.

### 5.2. Low-velocity CO (6–5) emission

In Fig. 10 we show the low-velocity channels in bins of 1  $\text{km s}^{-1}$  of the CO (6–5) emission in HH211-mm. At these low-velocity channels the outflow’s bipolar structure is clearly recognizable in all low-velocity channels. However, a more diffuse emission is also noted in channels 8  $\text{km s}^{-1}$  and 9  $\text{km s}^{-1}$  (i.e., around the cloud velocity,  $V_{\text{LSR}} = +9.2 \text{ km s}^{-1}$ ). We note that both outflow lobes are simultaneously present in channels 10 and 11  $\text{km s}^{-1}$ .

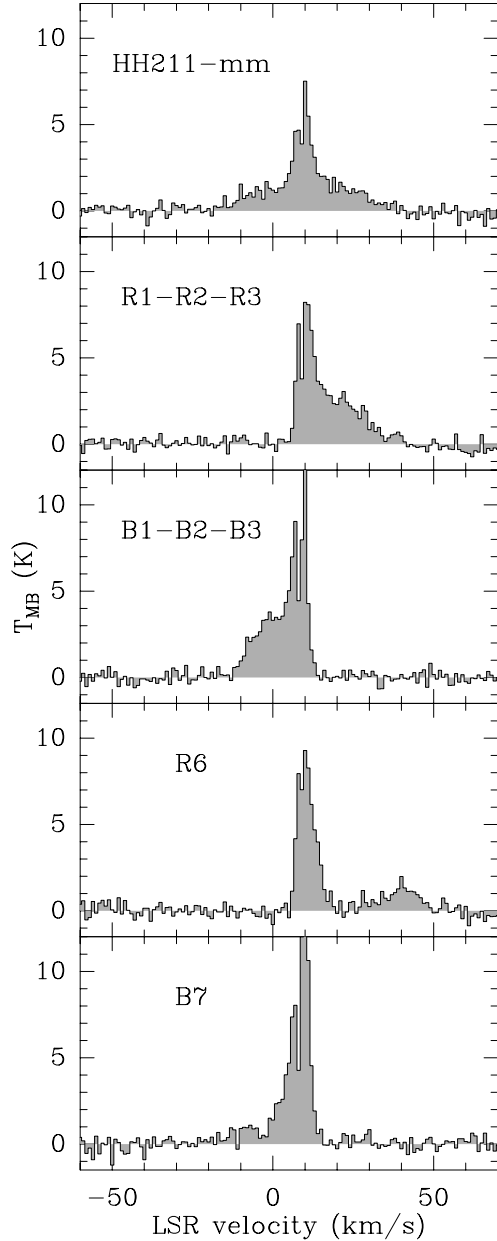


**Fig. 11.** CO (6–5) sample of spectra at selected positions in HH211. The spectral resolution is  $1 \text{ km s}^{-1}$ . Upper left corner of each panel indicates the position at which the spectrum was taken. The positions are also indicated in Fig. 9. The clumps B7 and R6 show secondary peaks at high velocities. The absorption feature at the cloud velocity ( $V_{\text{LSR}} = 9.2 \text{ km s}^{-1}$ ) is observed in all the positions shown here, which likely comes from the contamination of the reference position.

All emission clumps found at high velocities are also visible in the low-velocity emission.

### 5.3. CO(6–5) line profiles

Figure 11 shows a sample of spectra taken at the positions indicated in Fig. 9. Although at all positions the CO (6–5) emission peaks close to the cloud velocity, an important contribution from the high-velocity part of the spectra is noted as a broad “plateau” feature, from  $-14$  to  $+42 \text{ km s}^{-1}$ , towards the HH211-mm position. At this central position the CO (6–5) emission does not show secondary peaks at high velocities, as in the case of L1448-mm. This may be due to a projection effect, since the axis

of HH211 outflow is closer to the plane of the sky than in the case of L1448, which then causes the secondary peaks to “merge” with the broad “plateau” component. Another spectral feature is the wing-like emission at the B1-B2-B3 and R1-R2-R3 positions, which resembles the characteristic shock profile (i.e., slow decrease in intensity toward high velocities). In B1-B2-B3, the emission extends to  $\sim -10 \text{ km s}^{-1}$ , while in R1-R2-R3 it reaches  $\sim +40 \text{ km s}^{-1}$ . At the R6 position two spectral components are clearly defined: a narrow ( $FWHM \sim 5 \text{ km s}^{-1}$ ) and low-velocity ( $V_{\text{LSR}} \sim 9 \text{ km s}^{-1}$ ) component and a broad ( $FWHM \sim 10 \text{ km s}^{-1}$ ) and high-velocity ( $V_{\text{LSR}} \sim 40 \text{ km s}^{-1}$ ) component. The low-velocity component shows stronger emission ( $T_{\text{MB}} \sim 9 \text{ K}$ ) than the high-velocity one ( $T_{\text{MB}} \sim 2 \text{ K}$ ). An indication of a similar two-component feature is suggested in the spectrum at B7 position, but the high-velocity component is not as strong in intensity as in the R6 position. This two-velocity-component feature in the spectra at the apex positions is the mean difference between our mid- $J$  CO data and the previous low- $J$  CO observations, which only show a weak emission at this position (e.g. Lee et al. 2007, G99). Finally, at all positions shown in Fig. 11, a narrow absorption feature can be seen at around the cloud velocity. Although absorption features at cloud velocities have been found in observations of the same CO line in similar objects (e.g. van Kempen et al. 2009a; Yıldız et al. 2012), due to the contamination from the reference position in our observations of HH211 we cannot confidently determine whether or not these absorption features are due to a fore-ground cloud. Since this paper focuses mainly on the high-velocity gas related to the outflows, we do not discuss this absorption feature in detail.

### 5.4. $^{13}\text{CO}$ (6–5) and CO (7–6)

Figure 14 shows the  $^{13}\text{CO}$  (6–5) spectra taken at three different positions in HH211, namely HH211-mm, B7, and R6. Toward the HH211-mm position, the  $^{13}\text{CO}$  (6–5) emission is detected from  $7$  to  $14 \text{ km s}^{-1}$ , while around the B7 position the emission is present from  $7$  to  $11 \text{ km s}^{-1}$ . At R6, the  $^{13}\text{CO}$  (6–5) emission is only detected from  $9$  to  $11 \text{ km s}^{-1}$ . The spectra of the CO (7–6) emission at selected positions is shown in Fig. 12. The low-velocity CO (7–6) emission (from  $\sim 0 \text{ km s}^{-1}$  to  $10 \text{ km s}^{-1}$ ) is detected at all positions, and at high-velocities only toward B1-B2-B3 (up to  $\sim -10 \text{ km s}^{-1}$ ) and R1-R2-R3 (up to  $\sim +30 \text{ km s}^{-1}$ ). The integrated CO (7–6) map of the low-velocity range (where the emission is stronger) is presented in Fig. 13. The CO (7–6) map shows that the emission traces the same structures as are revealed by CO (6–5).

## 6. Optical depths

We estimated the  $^{12}\text{CO}$  (6–5) optical depth ( $\tau_{12}$ ) using the  $^{12}\text{CO}$  (6–5)/ $^{13}\text{CO}$  (6–5) line ratio. Assuming that the  $^{13}\text{CO}$  (6–5) is optically thin (which is usually the case for the line wings, e.g. Leurini et al. 2006), and that the  $^{12}\text{CO}$  (6–5) and  $^{13}\text{CO}$  (6–5) have the same excitation temperature, the following relation holds:

$$\frac{T_A^{12}}{T_A^{13}} = \frac{\nu_{12} [^{12}\text{CO}]}{\nu_{13} [^{13}\text{CO}]} \left( \frac{1 - e^{-\tau_{12}}}{\tau_{12}} \right). \quad (1)$$

In Eq. (1),  $T_A^{12}$  and  $T_A^{13}$  refer to the antenna temperature of  $^{12}\text{CO}$  (6–5) and  $^{13}\text{CO}$  (6–5) lines, with  $\nu_{12}$  and  $\nu_{13}$  their corresponding rest frequencies.  $[^{12}\text{CO}]/[^{13}\text{CO}]$  is the abundance ratio that in our case we assumed to be 62 (Langer et al. 1993). Therefore, Eq. (1) can be solved numerically to obtain  $\tau_{12}$ .

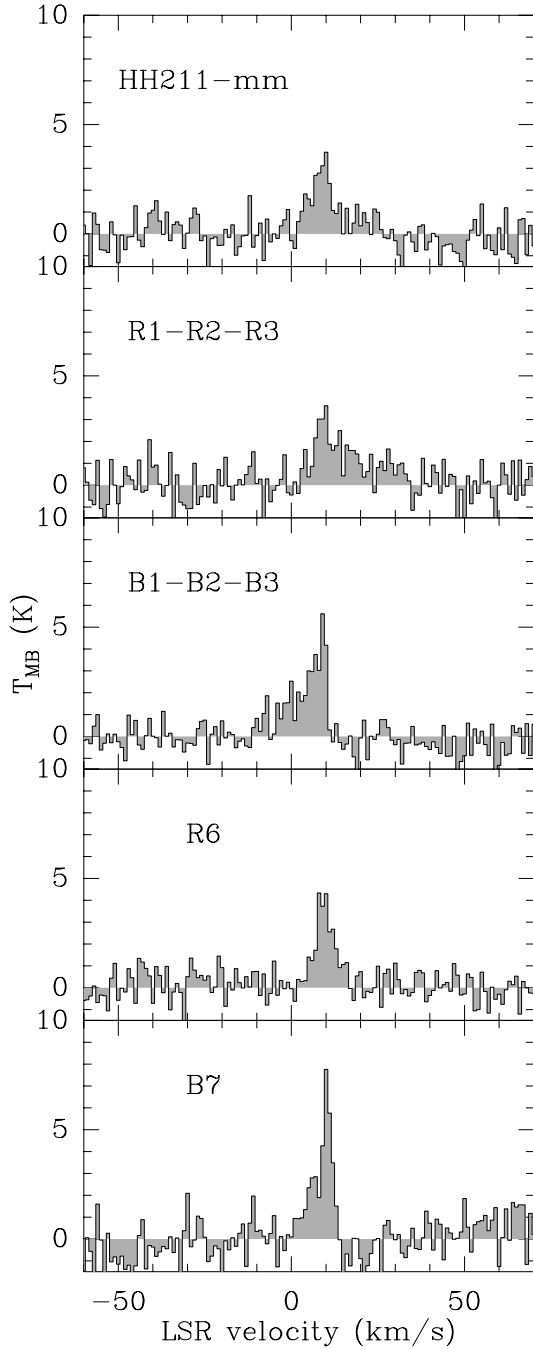


**Fig. 12.** CO (7–6) sample of spectra at selected positions in HH211. The spectral resolution is  $1 \text{ km s}^{-1}$ . Upper left corner of each panel indicates the position at which the spectrum was taken. The positions are also indicated in Fig. 9. The secondary peaks at high velocities revealed by the CO (6–5) transition are not detected in CO (7–6). The absorption feature at the cloud velocity, as in the case of the CO (6–5) emission, most likely comes from the contamination of the reference position.

From the spectra shown in Figs. 5 and 7, we computed the  $^{12}\text{CO}/^{13}\text{CO}$  (6–5) line ratio at different positions in L1448/IRS3. As already discussed, the  $^{13}\text{CO}$  (6–5) emission was mostly detected at low velocities, with its peak at the cloud velocity. In Table 4 we show the  $^{12}\text{CO}/^{13}\text{CO}$  (6–5) line ratio at the cloud velocity and the corresponding  $\tau_{12}$ . At the channel corresponding to the cloud velocity, the  $^{12}\text{CO}/^{13}\text{CO}$  (6–5) line ratio is in between 1.5–2.5 for L1448-mm, R1, R2, B3 and IRS3. Consequently,  $\tau_{12}$  is  $>30$ , and thus optically thick. On the other

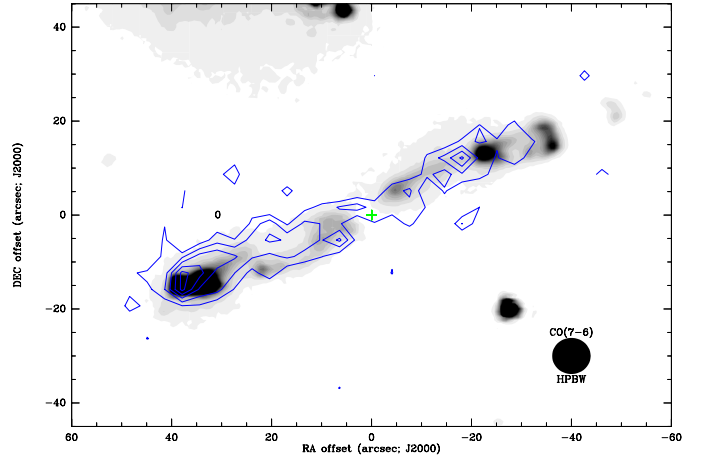


**Fig. 13.** CO (7–6) emission integrated from  $8 \text{ km s}^{-1}$  to  $12 \text{ km s}^{-1}$ . Contour spacing is  $1\sigma$  with the first contour at  $3\sigma$  ( $\sigma = 5.6 \text{ K km s}^{-1}$ ). The green plus symbol and gray scale are the same as in Fig. 9.

**Table 4.**  $^{12}\text{CO}$  opacities at the cloud velocity channel.

Position	$^{12}\text{CO}/^{13}\text{CO}$	$\tau_{12}$
L1448		
L1448-mm	2.2(0.2)	28.2
B1	8.5(1.6)	7.3
R1	1.8(0.1)	34.4
B2	$>41.9$	$<0.8$
R2	2.4(0.6)	25.8
B2-N	19.4(4.1)	3.0
B2-W	26.7(9.8)	2.0
B3	2.2(0.07)	28.2
B3-S	31.9(14.5)	1.5
IRS3	1.5(0.04)	41.3
HH211		
HH211-mm	1.5(0.2)	41.3
B7	7.6(1.0)	8.1
R6	4.3(0.6)	14.4

hand, at the positions where  $^{13}\text{CO}$  (6–5) was marginally detected around the cloud velocity (B1, B2-N, B2-W, and B3-S),  $\tau_{12}$  is in between 1–3, and therefore moderately optically thick. The upper limit computed around the extremely high-velocity range suggest that  $^{12}\text{CO}$  is at most moderately optically thick, i.e.,  $\tau_{12} < 6$  at R1 and  $\tau_{12} < 3$  at B1. At the position B2, where  $^{13}\text{CO}$  (6–5) was not detected at all, the upper limit indicates that the emission should be optically thin ( $^{12}\text{CO}/^{13}\text{CO}$  ratio  $>41$ , thus  $\tau_{12} < 0.8$ ). In summary, the information provided by the  $^{13}\text{CO}$  (6–5) observations indicates that the  $^{12}\text{CO}$  (6–5) low-velocity emission is optically thick around the central objects (L1448-mm and IRS3) and at R1, R2, and B3. On the other hand, at low velocities the  $^{12}\text{CO}$  (6–5) emission is moderately optically thick at B1, B2-N, B2-W, and B3-S, or even optically thin at B2. The upper limits for the extremely high-velocity gas suggest that the  $^{12}\text{CO}$  (6–5) emission is at most moderately optically thick ( $<5$ ) at these velocities.

From the  $^{12}\text{CO}$  and  $^{13}\text{CO}$  (6–5) spectra in Figs. 11 and 14, we calculated the  $^{12}\text{CO}/^{13}\text{CO}$  (6–5) line ratios at different positions in HH211. The line ratio values at the cloud velocity are presented in Table 4. The  $^{12}\text{CO}/^{13}\text{CO}$  (6–5) line ratios vary from 1.5 to 7.6 at the three different positions observed. These ratios indicate that  $\tau_{12}$  at the cloud velocity is  $\sim 41$ , 8, and 14, in HH211-mm, B7, and R6, respectively. Additionally, in channels adjacent to the cloud velocity,  $\tau_{12}$  can become as low as 10 and 3

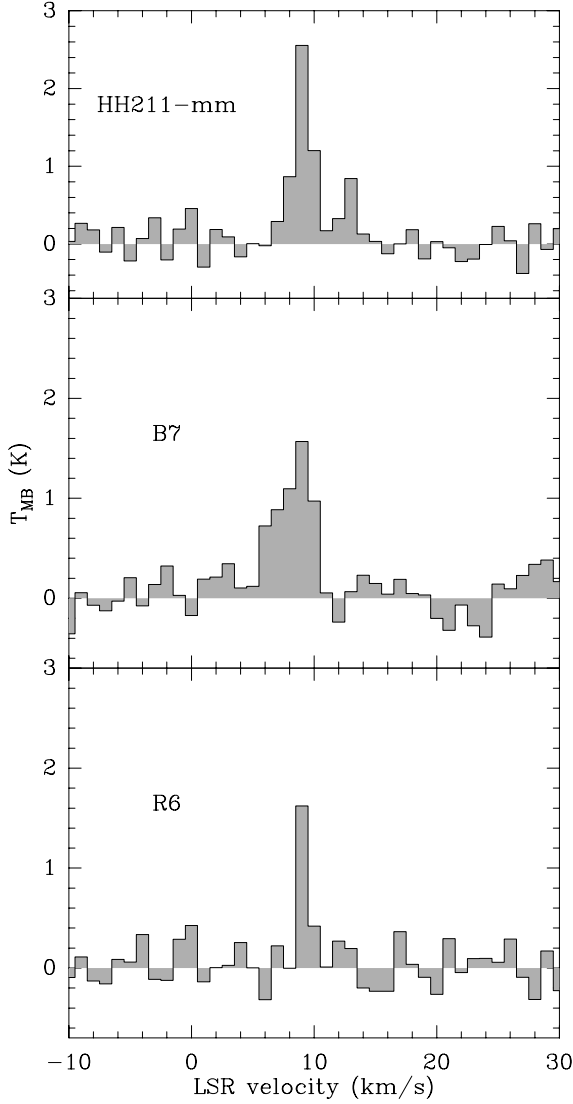


**Fig. 14.**  $^{13}\text{CO}$  (6–5) spectra at the positions HH211-mm, B7, and R6 (see Fig. 9). The spectral resolution is  $1 \text{ km s}^{-1}$ .

in HH211-mm and B7, respectively. These results show that the  $^{12}\text{CO}$  (6–5) line is optically thick at about the cloud velocity in HH211-mm, B7, and R6, while it can be moderately optically thick in adjacent channels in B7. Finally, upper limits to the  $^{12}\text{CO}$  opacity in the high-velocity gas are  $\leq 12$ , 13, and 8 for HH211-mm, B7, and R6, respectively. Therefore our  $^{13}\text{CO}$  (6–5) observation were not sensitive enough to prove whether or not the  $^{12}\text{CO}$  (6–5) emission is optically thin at high velocities.

The calculation of the  $^{12}\text{CO}$  opacities in L1448-mm/IRS3 and HH211-mm demonstrated that the CO (6–5) emission is optically thick around the central objects. On the other hand, the upper limits estimated for the high-velocity gas suggest that this emission is at most moderately optically thick in the outer line wings. Moreover, in the case of L1448-mm, even the low-velocity gas in the blue lobe presents moderately optically thick emission. In the following calculations for the outflow physical parameters we assume that the  $^{12}\text{CO}$ (6–5) emission at high velocities is optically thin. Thereafter, assuming an average optical depth from the upper limit calculations of the high-velocity range gives an estimate of the correction factor due to optical effects.

**Table 5.** CO integrated intensities and rotational diagram results the for B1 and R1 clumps in the L1448-mm outflow.

Velocity interval	$\int T dv(\sigma)$ (K km s $^{-1}$ )			$T_{\text{rot}}$ (km s $^{-1}$ )	$N_{\text{tot}}$ ( $10^{16} \text{ cm}^{-2}$ )
	4–3	6–5	7–6		
B1					
EHV	33.4(0.9)	21.8(0.7)	13.5(2.4)	77	1.6
Wing	86.6(1.2)	33.8(1.0)	13.2(3.1)	44	3.9
R1					
EHV	26.4(0.8)	19.8(0.9)	9.7(3.0)	71	1.3
Wing	138.1(1.1)	59.5(1.2)	30.0(4.0)	43	0.6

**Notes.** EHV:  $-45$  to  $-70 \text{ km s}^{-1}$  (B1);  $55$  to  $80 \text{ km s}^{-1}$  (R1). Wing:  $0$  to  $-44 \text{ km s}^{-1}$  (B1);  $10$  to  $54 \text{ km s}^{-1}$  (R1).

## 7. Excitation and physical conditions

### 7.1. Population diagram

We produced population diagrams to estimate the rotational temperature,  $T_{\text{rot}}$ . Under the assumption that the gas is in LTE, the population of each level follows the Boltzmann law, which in the optically thin case can be expressed as  $\log(N_u/g_u) = \log(N_{\text{tot}}/Q) - \log(e)/T_{\text{rot}}$ , where  $N_u$  and  $g_u$  are the column density and statistical weight of the upper state level, respectively,  $N_{\text{tot}}$  is the total column density, and  $Q$  the partition function (e.g. Goldsmith & Langer 1999).  $N_u$  is related to the integrated intensity ( $W$ ) by  $N_u = 8\pi k\nu^2 W/hc^3 A_{ul}$ , where  $k$  and  $h$  are Boltzmann and Planck constants, respectively,  $c$  is the speed of light,  $\nu$  the rest frequency, and  $A_{ul}$  the Einstein coefficient (see Table 1). The partition function is approximated by  $Q \sim T/(4.8 \times 10^{-2} B_e)$ , where  $B_e$  (57.6 GHz for CO) is the rotational constant (e.g. Rohlfs & Wilson 2004).

At the B1 and R1 positions in L1448-mm, complementary low- $J$  CO (4–3) observations are available in the literature (Nisini et al. 2000) and we used these in our calculations. We have then convolved our CO (6–5) and CO (7–6) observations to the same angular resolution of CO (4–3) observations, HPBW  $\sim 11''$  (Nisini et al. 2000). To compare with a previous analysis made on these positions by Tafalla et al. (2010), we divided the spectra at those positions into two velocity regimes: the extreme high velocity (EHV) ( $-45$  to  $-65 \text{ km s}^{-1}$  for B1,  $55$  to  $80 \text{ km s}^{-1}$  for R1), and the wing ( $0$  to  $-44 \text{ km s}^{-1}$  for B1,  $10$  to  $54 \text{ km s}^{-1}$  for R1). Table 5 shows the CO (4–3, 6–5, 7–6) integrated intensities at  $11''$  resolution together with the results of the rotational diagram. In Fig. 16 we also show graphically the results of the least-squares fits to the rotational diagrams for the two velocity regimes. Within the EHV range, a  $T_{\text{rot}}$  of  $\sim 77 \text{ K}$  and  $N \sim 1.6 \times 10^{16} \text{ cm}^{-2}$  is found for B1, while for R1 we obtain  $T_{\text{rot}} \sim 71 \text{ K}$  and  $N \sim 1.3 \times 10^{16} \text{ cm}^{-2}$ . On the other hand, the wing emission shows  $T_{\text{rot}}$  of  $\sim 44 \text{ K}$  and  $N \sim 3.9 \times 10^{16} \text{ cm}^{-2}$  for B1, while  $T_{\text{rot}} \sim 43 \text{ K}$  and  $N \sim 6.0 \times 10^{15} \text{ cm}^{-2}$  are found for R1. Therefore, a higher  $T_{\text{rot}}$  and a lower total column density are found in the EHV range than in the wing emission. This tendency was also found by Tafalla et al. (2010) with low- $J$  CO transitions. We note, however, that assuming the  $\tau_{12}$  upper limits for the EHV emission calculated in Sect. 6, the computed column densities would increase by a factor 6 and 3 for R1 and B1, respectively. We also point out that for the R2 and B2 positions where the EHV emission is seen in low- $J$  CO (e.g. Bachiller et al. 1990) but barely found in our mid- $J$  CO lines, the upper limits indicates that indeed the EHV gas at these positions should be less excited, with  $T_{\text{rot}} < 16 \text{ K}$  for R2 and  $T_{\text{rot}} < 31 \text{ K}$  for B2.

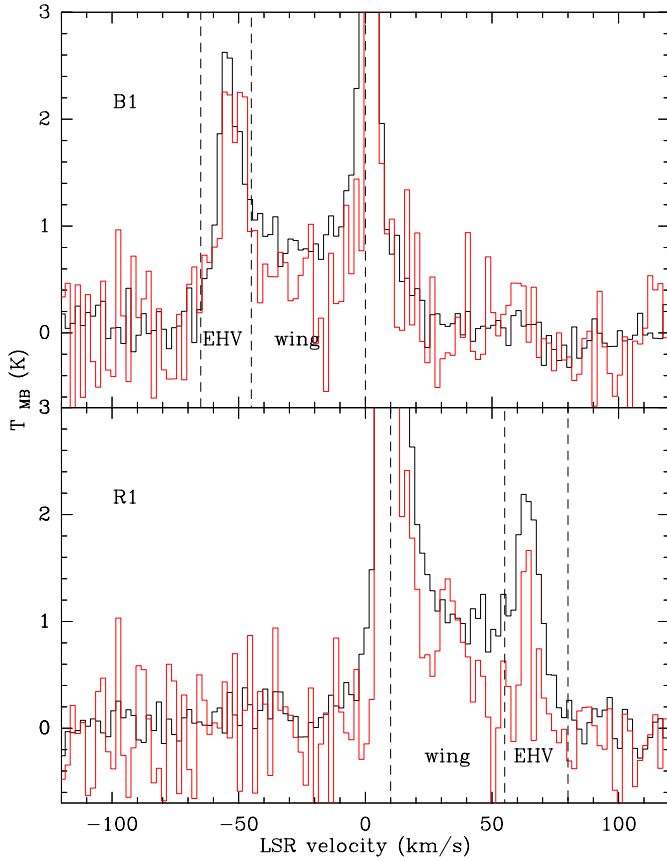


**Fig. 15.** CO 6–5 (black) and 7–6 (red) spectra ( $2 \text{ km s}^{-1}$  spectral resolution) at B1 and R1 positions in L1448-mm. Velocity ranges in which the emission is divided to study the physical conditions are indicated by vertical dashed lines (EHV and wing).

For all other positions in the L1448-mm outflow complementary CO (4–3) data are not available and the CO (7–6) emission at high-velocities is not strong enough to allow an analysis as a function of velocity range. Therefore, for these positions we used the total integrated intensities of CO (6–5) and (7–6) to produce the rotational diagram. The results of the least-squares fits to the rotational diagrams are shown in Table 6 together with the results obtained in the same way for the different positions in HH211-mm outflow. Note in particular the difference between the results of the total integrated emission and the results for the wing and EHV only presented in Table 5. Despite the beam-filling factor that most likely affects the EHV emission in the  $11''$  beam, a higher value of the rotational temperatures with respect to the total integrated or the wing emission is found. The column densities calculated from the rotational diagram analysis are used in the following non-LTE calculations.

## 7.2. Large velocity gradient

Radiative transfer calculations with RADEX (van der Tak et al. 2007) were made in the Large Velocity Gradient (LVG) approximation and plane-parallel geometry. The molecular data were retrieved from the LAMBDA data base<sup>2</sup>, which uses the energy levels, transition frequencies, and Einstein A coefficients from the CDMS and JPL catalogs. The collisional rate coefficients were adopted from Yang et al. (2010) and include energy levels up to  $J = 40$  for temperatures ranging from 2 K to 3000 K.

<sup>2</sup> <http://www.strw.leidenuniv.nl/~moldata/>

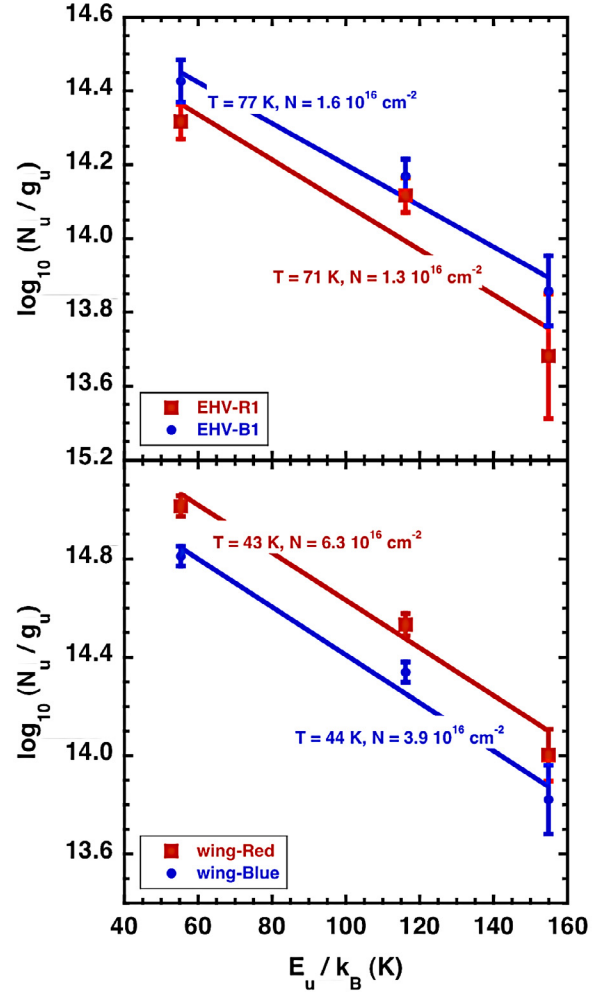


**Fig. 16.** Population diagram for the CO emission in the L1448 B1/R1 clumps. The *upper panel* shows the rotational diagram for the EHV range, while the *lower panel* corresponds to the wing range. Blue and red colors for symbols and lines represent B1 and R1, respectively.

*Thermal pressure.* A linear molecule such as CO can be a tracer of density or temperature. CO line ratios are density tracers at low densities, when collisions compete with radiative decay. At higher densities, the excitation becomes thermalized and the line ratios are sensitive to temperature (van der Tak et al. 2007). However, a quantity that can be better constrained by CO line ratios is the thermal pressure, defined as  $T_{\text{kin}} \times n$ , since usually ratios that use CO (6–5) and (7–6) transitions show a flatter curve than in a  $T_{\text{kin}}$  vs.  $n$  plot (see, e.g. van der Tak et al. 2007).

A series of LVG calculations were performed to reproduce the CO (6–5)/CO (7–6) line ratio at different positions within the outflow lobes. In our calculations we used the column densities previously derived from the rotational diagrams (Table 5). The results at some selected positions are shown in Fig. 17 as thermal pressure vs. temperature plots. Although the 6–5/7–6 line ratio cannot put severe constraints on the physical conditions of the clumps, a tendency of increasing thermal pressure toward positions farther away from the central object is suggested in L1448-mm (e.g. R4-S compared to B1). In the case of L1448-mm, a tendency of higher thermal pressure is suggested in the EHV gas (black line in Fig. 17) than in the total integrated emission (green line in Fig. 17). On the other

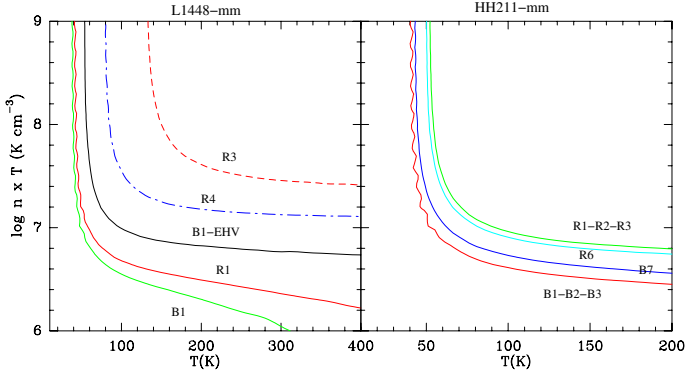


**Fig. 17.** Thermal pressure vs temperature plot from LVG calculations. The panels show the 6–5/7–6 observed ratios at different positions in L1448-mm (*left*) and in HH211-mm (*right*). With the exception of B1-EHV in L1448-mm, line ratios are computed from the total integrated emission.

**Table 6.** Rotational diagram results for total integrated intensities.

Position	$T_{\text{rot}}(\text{K})$	$N_T (10^{16} \text{ cm}^{-2})$
L1448-mm		
R1	$42 \pm 5\%$	$15.5 \pm 22\%$
B1	$38 \pm 6\%$	$13.1 \pm 23\%$
R2	$70 \pm 23\%$	$2.14 \pm 84\%$
B2	$39 \pm 11\%$	$5.24 \pm 41\%$
B2-N	$40 \pm 10\%$	$9.95 \pm 39\%$
B2-W	$53 \pm 9\%$	$5.00 \pm 34\%$
R3	$132 \pm 9\%$	$2.30 \pm 34\%$
R3-N	$129 \pm 8\%$	$2.31 \pm 31\%$
B3	$54 \pm 4\%$	$14.0 \pm 13\%$
B3-S	$40 \pm 13\%$	$8.39 \pm 49\%$
R4	$79 \pm 15\%$	$1.66 \pm 53\%$
R4-S	$70 \pm 11\%$	$2.96 \pm 40\%$
HH211-mm		
B1-B2-B3	$44 \pm 4\%$	$5.70 \pm 13\%$
R1-R2-R3	$52 \pm 10\%$	$4.25 \pm 40\%$
B7	$44 \pm 9\%$	$5.20 \pm 34\%$
R6	$50 \pm 10\%$	$2.74 \pm 35\%$

hand, in HH211-mm the thermal pressure seems to be no different than in the inner/outer positions, whereas a difference is observed between red- and blueshifted emission. A tendency of higher thermal pressure in the redshifted clumps compared to the blueshifted is suggested, as seen from Fig. 17.

*Spectral line energy distribution (SLED).* To study the role of the mid- $J$  CO lines in the context of the outflow’s physical components, we added the high- $J$  CO data observed with ISO to our LVG analysis (Nisini et al. 1999, 2000) as well as recent spectrally resolved Herschel CO (10–9) observations (Kristensen et al. 2011). Since the ISO observations were unable to resolve the EHV emission from B1 and R1 in space and velocity, only the combined emission from B1 and R1 could be used for the comparison with the mid- $J$  CO emission. We thus proceeded as in previous works, assuming that the ISO high- $J$  CO emission comes only from the EHV gas (Nisini et al. 2000), and sum up the EHV emission of B1 and R1 from our mid- $J$  CO data and the Herschel CO (10–9) spectrum to construct the CO-SLED shown in Fig. 18. Superimposed on the CO-SLED is the LVG solution that better fits the high- $J$  CO data, as found by Nisini et al. (2000), i.e.  $n_{\text{H}_2} \sim 6.5 \times 10^4 \text{ cm}^{-3}$  and  $T_{\text{kin}} \sim 1250 \text{ K}$ . However, this best fit to the high- $J$  CO data does not match the mid- $J$  CO observations. Indeed, this fit overpredicts the flux of the mid- $J$  CO lines, which indicates that this

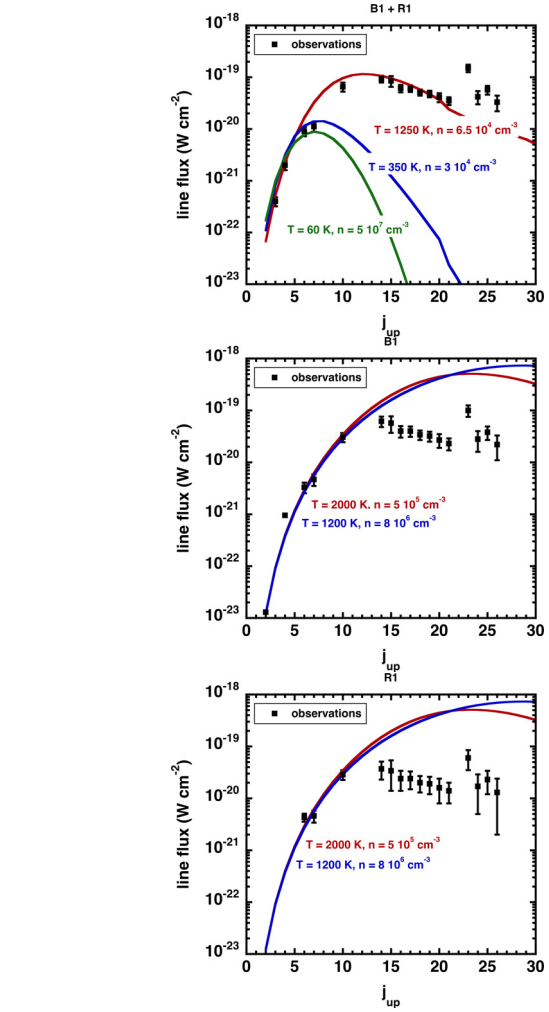


**Fig. 18.** LVG model fits to CO-SLED in the EHV range in L1448: combined B1 and R1 EHV emission (*upper panel*), B1 only (*middle panel*), and R1 only (*lower panel*). In the *upper panel* the red line shows the best fit to the ISO high- $J$ CO data, while blue and green show the fits to the low- and mid- $J$  CO data. In the *middle* and *lower panels* the red and blue lines show the best fits to the low- and mid- $J$  CO data points.

fit is incorrect, and that the mid- $J$  CO emission may be tracing a different component than the high- $J$  CO emission. The components that can explain the low- and mid- $J$  CO observations are indicated also in Fig. 18, showing that they trace lower temperatures (i.e.,  $T_{\text{kin}} \sim 60\text{--}350 \text{ K}$ ). Figure 18 also shows the CO-SLED for B1 and R1 separately and the LVG models that better fit the low- and mid- $J$  data points. For the high- $J$  CO lines the fluxes are scaled by a factor consistent with the ratio between B1 and R1 in CO (6–5). In both cases, temperatures  $>1200 \text{ K}$  and densities  $>5 \times 10^5$  are the conditions of the high-velocity gas. Again we see that the fits to low- and mid- $J$  CO data points miss the ISO high- $J$  CO data, but it is remarkable that the spectrally resolved HIFI CO (10–9) data point is consistent with this fit. Therefore, in the total integrated emission our observations are similar to the results obtained recently by other authors in other protostellar objects (van Kempen et al. 2010b; Herczeg et al. 2012; Yıldız et al. 2012; Manoj et al. 2013), i.e., that the high- $J$  and mid- $J$  CO lines trace two different components that are possibly related to two different physical processes. The exception is the EHV emission (which was not covered by previous studies), in which the mid- $J$  lines and high- $J$  CO (10–9) lines seems to trace the same component. New upcoming results from

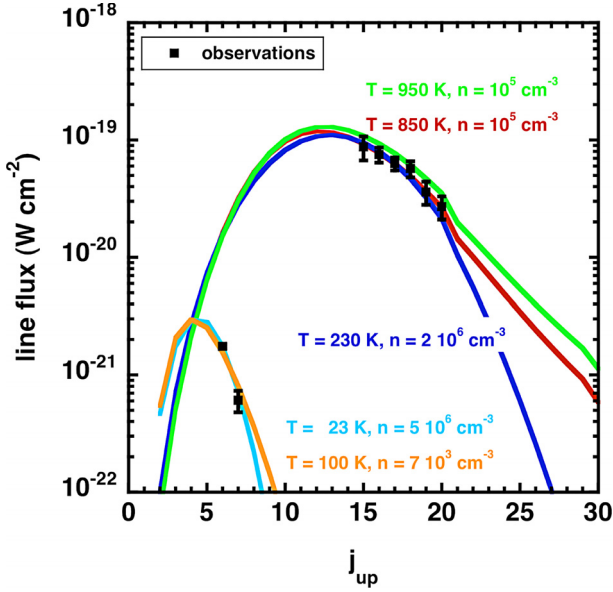


**Fig. 19.** LVG model fits to CO-SLED for the total integrated emission in HH211. Red, green, and blue show the LVG fits to the high- $J$  CO emission. Orange and light-blue lines are the LVG fits to the mid- $J$  CO emission.

Herschel/HIFI in additional high- $J$  CO lines will provide more information on this aspect.

We also constructed the CO-SLED around the central position of HH211-mm. ISO data were taken from [Giannini et al. \(2001\)](#), and we used the CO (6–5) and (7–6) total integrated emission around the central position. The resulting CO-SLED is shown in Fig. 19 along with different LVG models obtained with RADEX. The figure shows that the mid- and high- $J$  CO emission cannot be reproduced by the same LVG model. The high- $J$  CO emission is consistent with densities between  $8 \times 10^4$  to  $2 \times 10^6 \text{ cm}^{-3}$  and kinetic temperatures between 230 to 950 K (see also [Giannini et al. 2001](#)). On the other hand, mid- $J$  CO observations are consistent with densities of  $\sim 5 \times 10^4 \text{ cm}^{-3}$  and  $T_{\text{kin}} \sim 20 \text{ K}$ . We again have a similar situation as in L1448, in which mid- and high- $J$  CO emission cannot be explained by a single LVG model, which then may imply that they probably trace a different gas.

In the literature, only few protostellar outflows have reported CO observations from low- to high- $J$  ladders. Among them, recent examples that include Herschel high- $J$  CO and ground-based mid- $J$  CO observations are the low-mass outflows HH46 and HH52-54 ([van Kempen et al. 2010b](#); [Bjerkeli et al. 2011](#)). In both cases the CO SLEDs are fitted with at least two different components, although the fitted physical parameters are slightly different from our results for L1448 and HH211 (e.g., higher temperatures found in L1448/HH211 than in HH52-54).

## 8. Outflow properties

Using the velocity-integrated CO (6–5) maps (i.e., Fig. 2 and the right panel of Fig. 9) we calculated the outflow mass. In the optically thin case, the relation between the total column density ( $N$ ) with the velocity integrated emission ( $W$ ) is given by

$$N = \frac{1.4 \times 10^{14}}{(J+1)\mu^2 B_e} \frac{e^{(4.8 \times 10^{-2} B_e J(J+1)/T_{\text{ex}})}}{1 - e^{(-4.8 \times 10^{-2} \times 2 B_e J(J+1)/T_{\text{ex}})}} \times W, \quad (2)$$

which, for the CO (6–5), becomes

$$N(\text{CO}) = 3.92 \times 10^4 \frac{e^{82.94/T_{\text{ex}}}}{1 - e^{-33.18/T_{\text{ex}}}} \times W. \quad (3)$$

We used the standard ISM value for the relative  $^{12}\text{CO}$  abundance,  $X(\text{H}_2/\text{CO}) \sim 10^4$ , to obtain the  $\text{H}_2$  column density and finally calculated the  $\text{H}_2$  mass,

$$M = 2 \times m_{\text{H}} \times X(\text{H}_2/\text{CO}) \times \Omega \times N \times D^2. \quad (4)$$

Here,  $m_{\text{H}}$  is the hydrogen mass,  $\Omega$  the solid angle of the lobe, and  $D$  the distance to the source. Note that to correct for opacity effects, the above expression for the mass should be multiplied by  $\tau_{12}/(1 - e^{-\tau_{12}})$ . We measured  $\Omega \times N$  by summing the contribution of each pixel with a signal-to-noise ratio above 3. In the calculation we used a  $T_{\text{ex}}$  of 50 K for both outflows, i.e., an average temperature based on the results of the rotational diagram for the high-velocity gas (e.g. Table 5). For L1448-mm, with a total extension of 0.40 pc (blue: 0.19 pc, red: 0.21 pc) the total outflow mass is  $0.03 M_{\odot}$ . For HH211-mm, with an extension of 0.107 pc (blue: 0.058 pc, red: 0.049 pc), the total outflow mass is  $0.003 M_{\odot}$ . We also estimated the mass of the IRS3 outflow, assuming the same  $T_{\text{ex}} = 50 \text{ K}$ . In this case, the integrated intensity maps were computed from  $-20$  to  $+1 \text{ km s}^{-1}$  for the blueshifted emission and from  $25$  to  $9 \text{ km s}^{-1}$  for the redshifted emission. The total mass of IRS3 outflow is  $6.86\text{E-}3 M_{\odot}$ . The outflow mass assuming a  $T_{\text{ex}}$  of 50 K for all outflows are summarized in Table 7. Since it is possible that the emission in the low-velocity wings, which contribute considerable in total wing-integrated emission, maybe at least moderately optically thick, we assumed the average  $\tau_{12}$  values determined for the low-velocity emission (Sect. 6) and calculated the correction factor to the mass estimation to account for opacity effects. The average  $\tau_{12}$  is 3 for L1448/IRS3, while for HH211-mm the observations were not sensitive enough to provide a reliable value of the gas opacity. Therefore, accounting for opacity effects, the mass in L1448/IRS3 would be  $\sim 3$  times higher than the one computed assuming optically thin emission.

From previous CO (2–1) observations in L1448-mm the total mass was estimated to be  $0.056 M_{\odot}$  using a  $T_{\text{ex}}$  of about 15 K ([Bachiller et al. 1990](#)). In addition, measurements from the CO (3–2) line by [Curtis et al. \(2010\)](#) yield a total mass of  $0.15 M_{\odot}$  using a  $T_{\text{ex}}$  of 50 K and correcting for inclination and opacity effects. In our calculation for the outflow gas observed in CO (6–5) we obtained a mass of  $0.029 M_{\odot}$ . Therefore, the mass of the warm gas traced by our mid- $J$  CO observations is not significantly different (considering the errors and different calculation methods) with respect to mass inferred with low- $J$  CO transitions. The major discrepancy is with the CO (3–2) estimations of [Curtis et al. \(2010\)](#). However, accounting for the opacity effects that these authors took into account, but also the different velocity range of the integrated maps ([Curtis et al. 2010](#) considered velocities from  $2 \text{ km s}^{-1}$  away from the cloud velocity, while our maps include emission only from  $\sim 5 \text{ km s}^{-1}$  away from the cloud velocity), we found that the results would be similar (in total a factor of  $\sim 3 \times 1.3$  higher than the value reported without accounting for those effects for the opacity and velocity range). Similarly, CO (2–1) observations of the IRS3 outflow ([Kwon et al. 2006](#)) and CO (3–2) observations of the HH211 outflow ([Curtis et al. 2010](#)) reported mass estimates of  $0.003 M_{\odot}$  and  $0.009 M_{\odot}$ , respectively, which are similar within the errors to our results based on the CO (6–5) emission (see Table 7). A previous study by [van Kempen et al. \(2009a\)](#) in the low-mass outflow HH46 has shown the same trend, i.e., that when considering the errors and difference in the mass estimation method, low- $J$  and mid- $J$  CO lines yield similar results in the mass calculations.

We also determined other parameters such as the dynamical time scale ( $t_{\text{d}}$ ), the mass outflow rate ( $\dot{M}$ ), the mechanical force ( $F_{\text{m}}$ ), the kinetic energy ( $E_{\text{k}}$ ), and the mechanical

**Table 7.** Outflow properties derived from the CO (6–5) emission.

Vel range	$\delta_{\max}$ (km s <sup>-1</sup> )	$R_{\max}$ (10 <sup>-2</sup> pc)	$t_d$ (10 <sup>3</sup> yr)	$M(\text{H}_2)$ (10 <sup>-3</sup> $M_{\odot}$ )	$F_m$ ( $M_{\odot}$ km s <sup>-1</sup> yr <sup>-1</sup> )	$E_k$ (erg)	$L_{\text{mec}}$ ( $L_{\odot}$ )
L1448-mm							
Blue	69.5	19.0	2.67	16.7	4.34E-4	8.03E44	2.44
Red	75.5	21.0	2.72	12.6	3.50E-4	7.15E44	2.13
Total				29.3	7.84E-4	1.52E45	4.57
IRS3							
Blue	24.5	4.87	1.94	3.46	4.36E-5	2.07E43	0.086
Red	20.5	8.23	3.93	3.40	1.77E-5	1.42E43	0.029
Total				6.86	6.13E-5	3.49E43	0.115
HH211-mm							
Blue	23.2	5.80	2.45	1.62	1.54E-5	8.71E42	0.029
Red	32.8	4.90	1.46	1.13	2.53E-5	1.21E43	0.067
Total				2.75	4.07E-5	2.08E43	0.096

luminosity ( $L_{\text{mech}}$ ). We defined these quantities as follows:  $t_d = R_{\max}/\delta_{\max}$ ,  $\dot{M} = M/t_d$ ,  $P = M \times \delta_{\max}$ ,  $F_m = M \times \delta_{\max}/t_d$ ,  $E_k = M \times \delta_{\max}^2/2$ , and  $L_{\text{mech}} = E_k/t_d$  (e.g. [Beuther et al. 2002](#)). In the above expressions  $R_{\max}$  and  $\delta_{\max}$  are the maximum extension and maximum relative velocity of the lobes. Table 7 summarizes the results. In general, the estimated outflow parameters are, within the typical errors that include also opacity effects, consistent with previous results for other class 0/I objects (see, e.g., results from CO (3–2) data by [Curtis et al. 2010](#)). A more detailed discussion of the comparison of the outflow properties for our full sample (low-, intermediate-, and high-mass protostars) will be given in a forthcoming paper.

## 9. Comparison with mid-IR observations

Mid-IR observations with *Spitzer* have recently been used as a tool for studying shocks in a diverse range of objects (see, e.g. [Reach et al. 2006](#), [Smith et al. 2006](#)). For protostellar outflows, several low-mass protostars have been observed with the IRAC camera (e.g. [Seale & Looney 2008](#)). With four channels at 3.6, 4.5, 5.8 and 8.0  $\mu\text{m}$ , the IRAC camera covers several H<sub>2</sub> transitions (indeed, several transitions per channel) that can be excited in shocked regions in outflows. In particular, H<sub>2</sub> emission has been found to dominate band 2 (4.5  $\mu\text{m}$ ) emission ([Neufeld et al. 2009](#); [De Buizer & Vacca 2010](#)).

*Spitzer*/IRAC observations in L1448-mm have been presented previously by [Tobin et al. \(2007\)](#) and [Neufeld et al. \(2009\)](#). These observations indicate that in fact H<sub>2</sub> transitions dominate the emission in all four IRAC bands. However, a particular behavior of the L1448-mm outflow is that the emission in the red lobe is considerably weaker than the emission in blue lobe. A recent analysis by [Giannini et al. \(2011\)](#) performed on the H<sub>2</sub> line emission has proven that this behavior is produced by a difference in the properties of the gas in each of the outflow lobes. These authors found higher densities in the northern (blue) lobe, with a density peak close to the outflow tip and to the IRS3 source, with values close to 10<sup>7</sup> cm<sup>-3</sup>. In contrast, the southern lobe was found to have more constant density values that never exceed  $\sim(1-2) \times 10^6$  cm<sup>-3</sup>.

The CO (6–5) emission shows a similar morphology and brightness distribution to that of the mid-IR observations. Most of the CO (6–5) clumps have a counterpart in the mid-IR image of both HH211-mm and L1448-mm/IRS3. In particular, the clumps at the highest velocity range in L1448-mm are well correlated in position with the apex of each of the ejection events that are clearly traced by the mid-IR emission (see, e.g., the blue-lobe in the top-left panel of Fig. 3). Moreover, the

CO (6–5) emission in L1448-mm seems to be weaker in the red-lobe than in the blue-lobe, as is the case for the mid-IR emission. The CO (6–5) clumps in HH211-mm also present a counterpart in the mid-IR image, but a difference in the brightness distribution in red and blue lobes is not observed in either CO (6–5) or in mid-IR.

A more quantitative comparison can be made by contrasting the results of the rotational diagram analysis obtained from the mid-*J* CO emission and from the pure rotational H<sub>2</sub> lines in the mid-IR. Although the mid-IR H<sub>2</sub> rotational lines are tracing intrinsically warmer gas than the sub-millimeter CO rotational lines, and thus different excitation conditions than the latter, the trend of the variation of the rotational temperature through different positions can be compared. By using *IRS/Spitzer* spectroscopy data, [Dionatos et al. \(2009\)](#) have presented the mid-IR H<sub>2</sub> rotational diagram around four positions in L1448 (L1448-mm, B1, B2, and R1). We note that the rotational temperatures are similar in B1 and B2 as traced by H<sub>2</sub> ( $\sim 630$  K) and CO ( $\sim 40$  K). On the other hand, at the R1 position the H<sub>2</sub> rotational temperature is higher at R1 ( $\sim 900$  K) than at B1 and B2, while in CO the rotational temperature at R1 is similar to that at B1 and B2. HH211-mm has been observed with *IRS/Spitzer* in H<sub>2</sub> pure rotational transitions by [Dionatos et al. \(2010\)](#). Three positions in HH211-mm can be compared with our results, namely B1-B2-B3, B7, and R6. We note that the highest rotational temperature determined from H<sub>2</sub> is toward the position of clump R6 ( $\sim 1100$  K), while slightly lower temperatures are reported for B1-B2-B3 ( $\sim 860$  K) and B7 ( $\sim 980$  K). A similar trend is found from our analysis of the mid-*J* CO transitions, in which the rotational temperature is higher toward clump R6 ( $\sim 50$  K) than toward B1-B2-B3 and B7 (both with  $T_{\text{rot}} \sim 44$  K). We therefore see in both objects a similar trend in the change of the excitation condition as a function of position, as measured in our mid-*J* CO and in mid-IR pure rotational H<sub>2</sub> lines.

## 10. The CO (6–5) and (7–6) lines as tracers of the warm gas in outflows

The LVG results presented in Sect. 7.2 may support recent studies in other outflow sources in which the CO-SLED is explained only by invoking multiple physical components. The profiles of the CO-SLED shown here for HH211-mm and L1448-mm are similar to that shown for HH46 by [van Kempen et al. \(2010b\)](#). In HH46, the CO-SLED has been fitted with at least three physical components by these authors, with the low-*J* and mid-*J* CO dominated by passive and UV heating. However, to unambiguously assess this possibility for the sources under study in

this paper, complementary observations of higher- $J$  CO transitions are needed. Particular useful will be the observations of high- $J$  CO transitions with Herschel that are under way in some of the key programs. However, despite the lack of these observations, the CO (6–5) and (7–6) APEX data presented here show the relevance of such transitions, since as seen from the CO-SLED, they are close to the peak of a relatively warm component that is probably dominated by the passive and/or UV heating (see also van Kempen et al. 2010b).

Another important characteristic of the CO (6–5) and (7–6) emission in the outflows under study is that even at low velocities (i.e., close to the cloud velocity) the outflow region is still clearly visible, in contrast to low- $J$  CO observations, in which the low-velocity emission from the cloud drastically hides the low-velocity emission from the outflow. In the particular case of L1448-mm/IRS3, in which our observations provide a high enough spatial resolution, more CO clumps than previously reported in low- $J$  CO have been found through the CO (6–5) low-velocity emission. Some of these clumps may be related with the L1448-mm main outflow or with the outflows from the IRS3 system.

Finally, we have also shown that the CO (6–5) and (7–6) emission is a particular tracer of terminal bow shocks. In L1448-mm, the terminal bow-shock at R4-S position is brighter in CO (6–5) than in low- $J$  CO observations. At the terminal bow-shock positions B7 and R6 in HH211-mm a similar behavior was found. From the LVG calculations we have shown that at these positions a higher thermal pressure occurs, than at other positions inside the outflow lobes.

## 11. Summary and conclusions

In the following we summarize the main results from this study:

1. The CO (6–5)/(7–6) emission in L1448-mm/IRS3 and HH211-mm was found to be tracing the low- and high-velocity emission from the outflows related to these objects.
2. The extremely high velocity emission in L1448-mm was detected in both CO (6–5) and (7–6) transitions from the clumps inside a radius of about  $10''$  from the central object.
3. High-velocity emission was detected in CO (6–5) around the central source in HH211-mm and also at the bow-shock positions.
4. By a comparison with previous observations we found that the mid- $J$  CO (6–5)/(7–6) emission is stronger toward the central region of L1448-mm than the low- $J$  CO emission. Similarly, the terminal bow shocks in both objects are stronger in mid- $J$  CO (6–5)/(7–6) than in low- $J$  CO.
5. The LVG model that fits the mid- $J$  CO emission in L1448-mm shows that the densities and kinetic temperatures of this EHV gas are  $n > 5 \times 10^5 \text{ cm}^{-3}$  and  $T_{\text{kin}} > 1200 \text{ K}$ .
6. An LVG analysis that includes far-IR CO lines from ISO shows that it is not possible to simultaneously fit the mid- $J$  and high- $J$  CO lines with only one component for both the L1448-mm and HH211-mm outflows. This may support recent studies that proposed that multiple physical components generate the CO-SLED around the central regions in protostellar outflows.
7. In both outflows, the outflow structures are clearly seen even around the cloud velocity, in contrast with low- $J$  CO observations, in which the low-velocity gas from the outflow is hidden by the emission from the cloud.

8. Complementary observations of far-IR CO lines are needed to separate the different emission components at work in protostellar outflows.

*Acknowledgements.* We wish to thank the whole APEX staff in Chile for their enthusiastic help during these observations. We are grateful to the referee, T. van Kempen, for the detailed comments which improved this paper. A.G.R. was supported by a stipend from the International Max-Planck Research School for Astronomy and Astrophysics at the universities of Bonn and Cologne. We thank B. Nisini, A. Palau, and L. Kristensen for providing parts of the complementary data presented in this paper, and also A. Belloche and B. Parise for their help with the data reduction and analysis.

## References

- Arce, H. G., Shepherd, D., Gueth, F., et al. 2007, *Protostars and Planets V*, 245  
 Bachiller, R., & Cernicharo, J. 1986, *A&A*, 168, 262  
 Bachiller, R., Martin-Pintado, J., Tafalla, M., Cernicharo, J., & Lazareff, B. 1990, *A&A*, 231, 174  
 Bachiller, R., Andre, P., & Cabrit, S. 1991, *A&A*, 241, L43  
 Beuther, H., Schilke, P., Sridharan, T. K., et al. 2002, *A&A*, 383, 892  
 Bjerkeli, P., Liseau, R., Nisini, B., et al. 2011, *A&A*, 533, A80  
 Curtis, E. I., Richer, J. S., Swift, J. J., & Williams, J. P. 2010, *MNRAS*, 408, 1516  
 De Buizer, J. M., & Vacca, W. D. 2010, *AJ*, 140, 196  
 Dionatos, O., Nisini, B., Garcia Lopez, R., et al. 2009, *ApJ*, 692, 1  
 Dionatos, O., Nisini, B., Cabrit, S., Kristensen, L., & Pineau Des Forêts, G. 2010, *A&A*, 521, A7  
 Enoch, M. L., Young, K. E., Glenn, J., et al. 2006, *ApJ*, 638, 293  
 Froebrich, D. 2005, *ApJS*, 156, 169  
 Giannini, T., Nisini, B., & Lorenzetti, D. 2001, *ApJ*, 555, 40  
 Giannini, T., Nisini, B., Neufeld, D., et al. 2011, *ApJ*, 738, 80  
 Goldsmith, P. F., & Langer, W. D. 1999, *ApJ*, 517, 209  
 Gueth, F., & Guilloteau, S. 1999, *A&A*, 343, 571  
 Güsten, R., Nyman, L. Å., Schilke, P., et al. 2006, *A&A*, 454, L13  
 Herczeg, G. J., Karska, A., Bruderer, S., et al. 2012, *A&A*, 540, A84  
 Hirano, N., Liu, S.-Y., Shang, H., et al. 2006, *ApJ*, 636, L141  
 Hirota, T., Honma, M., Imai, H., et al. 2011, *PASJ*, 63, 1  
 Kasemann, C., Güsten, R., Heyminck, S., et al. 2006, in *SPIE Conf. Ser.*, 6275  
 Kawamura, J. H., Hunter, T. R., Tong, C.-Y. E., et al. 1999, *PASP*, 111, 1088  
 Klein, B., Philipp, S. D., Krämer, I., et al. 2006, *A&A*, 454, L29  
 Kristensen, L. E., van Dishoeck, E. F., Tafalla, M., et al. 2011, *A&A*, 531, L1  
 Kwon, W., Looney, L. W., Crutcher, R. M., & Kirk, J. M. 2006, *ApJ*, 653, 1358  
 Langer, W. D., Wilson, R. W., & Anderson, C. H. 1993, *ApJ*, 408, L45  
 Lee, C.-F., Ho, P. T. P., Palau, A., et al. 2007, *ApJ*, 670, 1188  
 Leurini, S., Schilke, P., Parise, B., et al. 2006, *A&A*, 454, L83  
 Manoj, P., Watson, D. M., Neufeld, D. A., et al. 2013, *ApJ*, 763, 83  
 McCaughrean, M. J., Rayner, J. T., & Zinnecker, H. 1994, *ApJ*, 436, L189  
 Neufeld, D. A., Nisini, B., Giannini, T., et al. 2009, *ApJ*, 706, 170  
 Nisini, B., Benedettini, M., Giannini, T., et al. 1999, *A&A*, 350, 529  
 Nisini, B., Benedettini, M., Giannini, T., et al. 2000, *A&A*, 360, 297  
 Nisini, B., Codella, C., Giannini, T., & Richer, J. S. 2002, *A&A*, 395, L25  
 Palau, A., Ho, P. T. P., Zhang, Q., et al. 2006, *ApJ*, 636, L137  
 Rohlfs, K., & Wilson, T. L. 2004, *Tools of radio astronomy*, eds. K. Rohlfs, & T. L. Wilson  
 Schilke, P., Walmsley, C. M., Pineau des Forets, G., & Flower, D. R. 1997, *A&A*, 321, 293  
 Seale, J. P., & Looney, L. W. 2008, *ApJ*, 675, 427  
 Smith, H. A., Hora, J. L., Marengo, M., & Pipher, J. L. 2006, *ApJ*, 645, 1264  
 Tafalla, M., Santiago-García, J., Hacar, A., & Bachiller, R. 2010, *A&A*, 522, A91  
 Tobin, J. J., Looney, L. W., Mundy, L. G., Kwon, W., & Hamidouche, M. 2007, *ApJ*, 659, 1404  
 van der Tak, F. F. S., Black, J. H., Schöier, F. L., Jansen, D. J., & van Dishoeck, E. F. 2007, *A&A*, 468, 627  
 van Kempen, T. A., van Dishoeck, E. F., Güsten, R., et al. 2009a, *A&A*, 507, 1425  
 van Kempen, T. A., van Dishoeck, E. F., Güsten, R., et al. 2009b, *A&A*, 501, 633  
 van Kempen, T. A., Green, J. D., Evans, N. J., et al. 2010a, *A&A*, 518, L128  
 van Kempen, T. A., Kristensen, L. E., Herczeg, G. J., et al. 2010b, *A&A*, 518, L121  
 Yang, B., Stancil, P. C., Balakrishnan, N., & Forrey, R. C. 2010, *ApJ*, 718, 1062  
 Yıldız, U. A., Kristensen, L. E., van Dishoeck, E. F., et al. 2012, *A&A*, 542, A86